

Structure of the Airflow above Surface Waves

MARC P. BUCKLEY* AND FABRICE VERON

College of Earth, Ocean, and Environment, University of Delaware, Newark, Delaware

(Manuscript received 20 July 2015, in final form 2 February 2016)

ABSTRACT

In recent years, much progress has been made to quantify the momentum exchange between the atmosphere and the oceans. The role of surface waves on the airflow dynamics is known to be significant, but our physical understanding remains incomplete. The authors present detailed airflow measurements taken in the laboratory for 17 different wind wave conditions with wave ages [determined by the ratio of the speed of the peak waves C_p to the air friction velocity u_* (C_p/u_*)] ranging from 1.4 to 66.7. For these experiments, a combined particle image velocimetry (PIV) and laser-induced fluorescence (LIF) technique was developed. Two-dimensional airflow velocity fields were obtained as low as $100\ \mu\text{m}$ above the air–water interface. Temporal and spatial wave field characteristics were also obtained. When the wind stress is too weak to generate surface waves, the mean velocity profile follows the law of the wall. With waves present, turbulent structures are directly observed in the airflow, whereby low-horizontal-velocity air is ejected away from the surface and high-velocity fluid is swept downward. Quadrant analysis shows that such downward turbulent momentum flux events dominate the turbulent boundary layer. Airflow separation is observed above young wind waves ($C_p/u_* < 3.7$), and the resulting spanwise vorticity layers detached from the surface produce intense wave-coherent turbulence. On average, the airflow over young waves (with $C_p/u_* = 3.7$ and 6.5) is sheltered downwind of wave crests, above the height of the critical layer z_c [defined by $\langle u(z_c) \rangle = C_p$]. Near the surface, the coupling of the airflow with the waves causes a reversed, upwind sheltering effect.

1. Introduction

Small-scale dynamics at the wavy air–sea interface strongly influence the exchanges of heat, momentum, mass, and energy between the ocean and the atmosphere. These fluxes may in turn impact large-scale weather patterns, sea state, and climate and are, as such, key components of recent oceanic and atmospheric models (e.g., Breivik et al. 2015). The complex feedback mechanisms involved in the coupling between wind and waves and their effects on the atmospheric and oceanic boundary layers have recently received

increased interest, particularly in the context of extreme weather forecasts and climate predictions (e.g., Chen et al. 2013).

In recent years, efforts to estimate drag coefficients at the ocean surface have revealed that drag depends not only on wind speed, but also on wave height, wave slope, wind wave alignment, and wave age (e.g., Donelan et al. 1995; Jones and Toba 2001; Sullivan and McWilliams 2010). Wave age is important because it is a direct indicator of the coupling between the wind and the waves, which is crucial for determining the total momentum flux at the ocean surface. Wave age is generally defined as C_p/u_* or C_p/U_{10} . It is the phase speed of the peak waves C_p , normalized by the 10-m wind speed U_{10} or by the air friction velocity u_* . In fetch-limited, “local equilibrium conditions” (Csanady 2001), strongly forced short wind waves move slowly compared to the speed of the wind: they are young. Long swells often move fast with respect to wind speed: they are old. In these idealized conditions, young waves are found at shorter fetches, while older waves are found at longer fetches. The frequency spectrum of waves in the ocean has been found to reach a state of saturation or “wind-wave

 Denotes Open Access content.

* Current affiliation: Institute of Coastal Research, Helmholtz-Zentrum Geesthacht, Geesthacht, Germany.

Corresponding author address: Marc Buckley, Institute of Coastal Research, Helmholtz-Zentrum Geesthacht, Max-Planck-Str. 1, 21502 Geesthacht, Germany.
E-mail: mbuckley@udel.edu

DOI: 10.1175/JPO-D-15-0135.1

equilibrium” (Sullivan and McWilliams 2010), when $C_p/U_{10} \sim 1.2$ (Alves et al. 2003). This is when the spectral density of the wave field reaches an upper limit, because energy dissipation processes are balancing the energy input from the wind (Phillips 1977). Young seas with wave ages C_p/U_{10} below 1.2 are often considered to be in a “wind-driven wave regime,” and when $C_p/U_{10} > 1.2$, the wind is “wave driven” (Sullivan and McWilliams 2010).

Modelers have suggested that wind–wave coupling mechanisms differ significantly from one regime to another (Belcher and Hunt 1993; Sullivan et al. 2000; Kihara et al. 2007), but experimental evidence is scarce, and wave growth mechanisms are still not fully understood (Belcher and Hunt 1998; Sullivan and McWilliams 2010). In particular, two competing theoretical approaches have been the subject of vigorous debate: Miles’s (1957) quasi-laminar critical layer wave generation theory and Belcher and Hunt’s (1993) sheltering hypothesis. In Miles’s (1957) theory, which is based on linear stability analysis of a stratified shear flow, turbulent (and viscous) stresses are considered negligible very close to the water surface, and waves generate an air-side shear instability that in turn causes wave growth. Belcher and Hunt (1993), on the other hand, suggested that turbulent stresses above waves are spatially distributed in such a way (with respect to wave phase) that they force a “thickening of the boundary layer” (Belcher and Hunt 1993) downwind of the average wave, which is favorable to wave growth. As emphasized by Sullivan and McWilliams (2010), this mechanism is common in aerodynamics, where an average thinning (thickening) of a turbulent boundary layer is known to occur upstream (downstream) of a blunt object. In the case of waves, this implies a wave-coherent distribution of form and viscous shear stresses along the wave profile, which are both favorable to wave growth. In fact, the along-wave distribution of viscous stress has been suggested by Longuet-Higgins (1969) to have the same dynamical effects on wave growth as wave-coherent normal stresses (with a $\pi/2$ phase lag). But when turbulence is included in a wind–wave coupling theory, the closure problem requires a modeling effort that can only be validated by turbulence measurements above actual waves (e.g., Hsu et al. 1981). Surface gravity waves affect the turbulence in the airflow in such a way that measurements of turbulence over solid wavy boundaries (e.g., Kendall 1970) are not quite sufficient to address this need. In fact, the mechanisms by which momentum is transferred across the air–sea interface are further complicated not only by wave breaking and sea spray generation, but also by the intermittent occurrence of airflow separation events,

which may strongly impact the air–sea momentum flux (Banner and Melville 1976), and start to be significant even in low to moderate wind speeds (see, e.g., Veron et al. 2007; this study).

Direct numerical simulations (DNSs) have provided details of the airflow structure (Sullivan et al. 2000; Yang and Shen 2010), and some have supported Belcher and Hunt’s (1998) prediction that Miles’s (1957) critical layer mechanism may be important for wave growth for intermediate wave ages ($15 \leq C_p/u_* \leq 25$), whereas turbulence-driven sheltering effects dominate for young ($C_p/u_* \leq 15$) and for old waves ($C_p/u_* \geq 25$; Kihara et al. 2007). However, because of high computational costs, DNS studies have been restricted to idealized monochromatic waves. Other modeling efforts focused on parameterizing wind wave momentum fluxes over more realistic wide-spectrum wave fields (e.g., Makin et al. 1995; Hara and Belcher 2002; Mueller and Veron 2009). Their results suggest that the turbulent shear stress is reduced by the presence of the wave field and replaced by wave-coherent stress. More recently, modelers were able to integrate realistic complex wave fields into large-eddy simulations (LESs) that yielded insight on the instantaneous turbulent structure of the airflow over a wide range of wave ages (Sullivan et al. 2014), including very old waves (Sullivan et al. 2008) where upward wave-induced momentum flux was observed, as well as wave-driven jets, in agreement with field observations by Smedman et al. (1999) and Grachev and Fairall (2001). Using LES within the wave boundary layer over young wind-forced sinusoidal waves, Hara and Sullivan (2015) were able to estimate the wave-induced and turbulent components of the wind stress and their influence on the total drag.

Recent field observations have been largely of two kinds. The first, focused on turbulent flux measurements and efforts to parameterize drag as a function of wind speed (e.g., Edson et al. 2013), were motivated by a need to rapidly improve operational forecasting and climate modeling (see, e.g., the COARE momentum flux model; Webster and Lukas 1992). Others, concerned with the fundamental physics of wave generation and growth mechanisms, were able to relate their flux measurements to the phase of the waves, thereby estimating wave-coherent fluxes, which provided evidence of Miles’s critical layer mechanism for a certain range of wave ages (Hristov et al. 2003; Grare et al. 2013a). However, these field studies, challenged by the technical difficulties involved with the study of small-scale dynamics in the open ocean near a highly dynamic interface, were limited to fixed-height vertical profile measurements some distance above the level of the highest wave crest. In such conditions, it is difficult to

understand the near-surface airflow dynamics, and in particular the distortion of the turbulence by the wave field below.

Laboratory measurements, also technically challenging, have attempted to fill this knowledge gap. Hsu et al. (1981) observed a strong modulation of the wave-coherent stress by the wave-coherent turbulent stress, but their data were obtained over idealized mechanically generated waves. Using laboratory measurements, Mastenbroek et al. (1996) found evidence that rapid distortion (Batchelor and Proudman 1954) of the turbulence occurs above the critical layer, which has important implications on turbulence closure models and, in particular, questions the validity of the commonly used eddy-viscosity-type closure. Later, two-dimensional near-surface airflow measurements were achieved using particle image velocimetry, and single airflow separation events were directly observed by Reul et al. (1999, 2008) over steep, mechanically generated breaking waves and by Veron et al. (2007) over wind waves. Recently, Grare et al. (2013b), using single point probes, were able to estimate viscous stress in the air above laboratory wind-generated waves and suggested an important relative contribution of viscous stress with respect to the total air–water momentum flux, which has been the subject of debate over the past decades (e.g., Okuda et al. 1977; Banner 1990; Banner and Peirson 1998; Grare et al. 2013b).

In this paper, we present high-resolution, two-dimensional measurements of the airflow above waves, obtained in the laboratory, using a complex experimental system specially developed for this study (see section 2). The instantaneous turbulent structure of the airflow contains features reminiscent of turbulent boundary layers over flat plates (e.g., ejections and sweeps paired with detached high vorticity layers) and over solid wavy boundaries (e.g., airflow separation), but the water surface dynamics associated with this moving, wavy, free surface also dramatically influence the turbulent airflow, starting at relatively low wave ages ($C_p/u_* = 6.5$). Our results, presented alongside mean wave-coherent velocities and momentum fluxes in section 3, point to the complex interactions between mean and instantaneous turbulent effects on wind–wave coupling, which in turn may impact the total flux. Finally, we summarize our contributions to the topic in section 4.

2. Methods

The experiments presented in this paper were conducted in the large wind–wave–current tank at the Air–Sea Interaction Laboratory of the University of Delaware. The tank, designed and equipped for air–sea

interaction studies, is sketched in Fig. 1a. The tank is 42 m long, 1 m wide, and 1.25 m high. Water depth was kept at 0.70 m. The tank is equipped with a programmable, computer-controlled, recirculating wind tunnel, which, for these experiments, generated 10-m equivalent wind speeds ranging from 0.86 to 16.63 m s^{-1} . Mean experimental conditions are listed in Table 1. In some cases, the waves were solely wind generated. In other cases, wind waves were combined with longer mechanically generated regular (MGR) waves (Bliven et al. 1986) to simulate swells. These MGR waves were produced by a plunging wedge mechanical wave maker. Figure 1b shows a sketch of the instrument setup, positioned at a fetch of 22.7 m. A complex imaging system was specifically developed for this study. Using a combination of particle image velocimetry (PIV) and laser-induced fluorescence (LIF) techniques, we were able to measure velocities in the air above waves, on average as close as 100 μm to the air–water interface. In addition to wind velocities, temporal and spatial wave properties were measured by LIF simultaneously with the velocity measurements. Details are provided in the following sections.

To be able to easily compare wind waves and MGR waves, and to illustrate the coupling between the waves and the wind, we will generally present our results as a function of wave age C_p/u_* . Also, waves and mean winds are propagating in the positive x direction (and positive phase) and will be systematically plotted in all figures traveling from left to right.

a. Measurement of wave properties

Two types of wave data were collected during these experiments: single-point, high-frequency wave height measurements and spatial surface profiles with high spatial resolution. Time series of the water height were obtained using four single-point optical wave gauge (WG) systems (Figs. 1b,c), positioned respectively 2.8 and 1.4 cm upwind and 2.7 and 4.2 cm downwind of the PIV field of view. The wave gauge systems consisted of two charge-coupled device (CCD) cameras (300×1600 pixels, model JAI CV-M2), fitted with amber acrylic bandpass filters (566 nm), each of which imaged the intersection of two 200-mW continuous green laser beams with the surface. Rhodamine 6G dye was added to the water at a concentration of $8 \times 10^{-6} \text{ g L}^{-1}$. The resulting LIF images provided measurements of the water height with a resolution of 65 μm , and at a frequency of 93.6 Hz. Large along-channel spatial profiles of the wavy surface were also obtained by LIF, using a large-field-of-view (LFV) CCD camera (2048×2048 pixels, model JAI RM-4200) that was focused on the intersection of a large green laser sheet, generated by a pulsed neodymium-doped yttrium aluminum garnet (Nd:YAG) laser

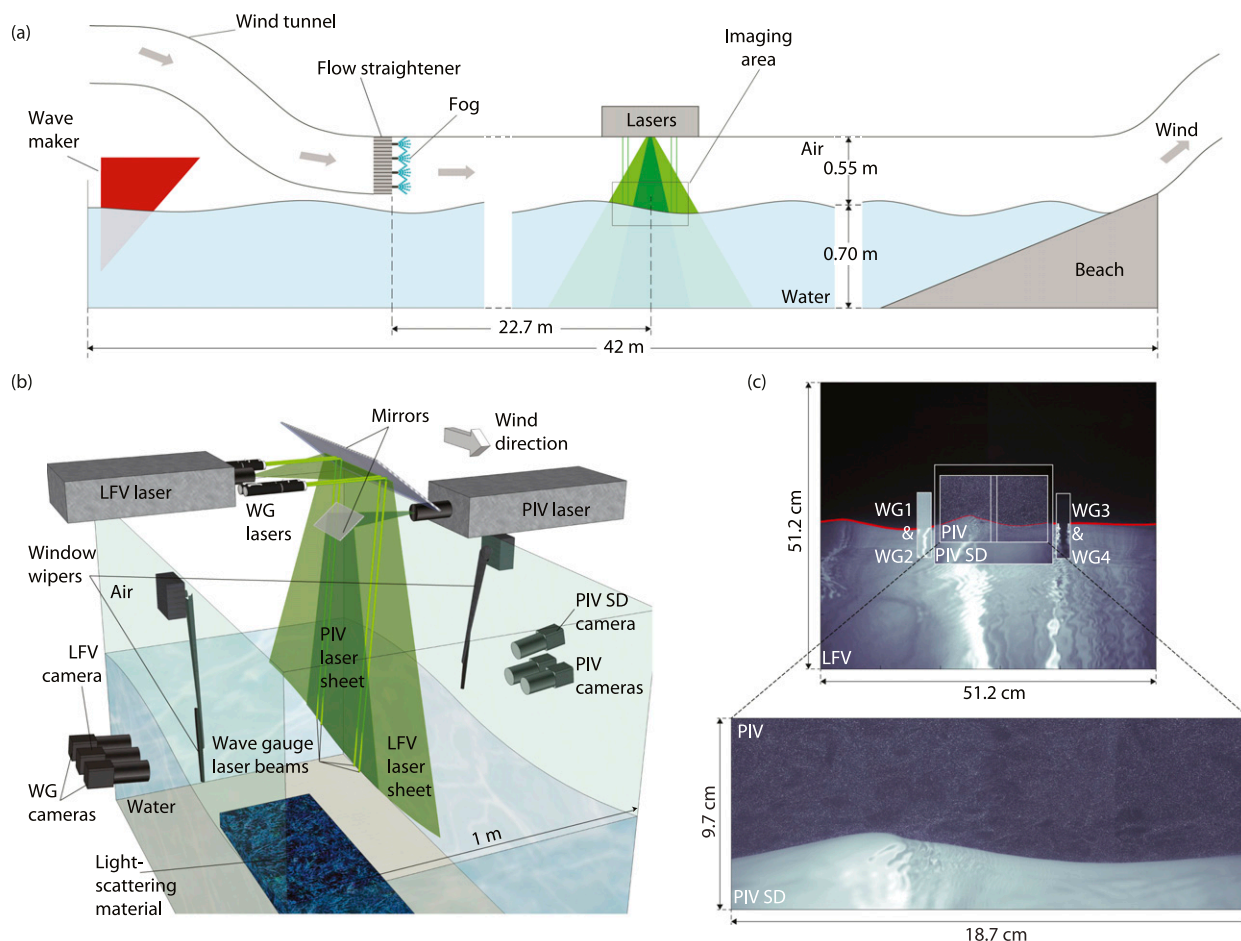


FIG. 1. (a) Sketch of the large recirculating wind-wave-current tank at the University of Delaware's Air-Sea Interaction Laboratory. The location of the experimental setup is shown. The center of the imaging area is located at a fetch of 22.7 m. The airflow is conditioned (airflow straightener) and seeded (fog) at the location of zero fetch. (b) A 3D sketch of the wind-wave imaging system. The airflow velocity measurement system is on the right-hand side. It is a combination of PIV and PIV SD. Both make use of the PIV laser sheet for illumination. The PIV uses direct laser light reflection on the fog particles; the PIV SD uses fluorescence of the rhodamine 6G present in the water. The wave field measurement system is on the left and consists of an LFV spatial wave profile imager and four single-point laser WG systems. Both LFV and WG are using laser-induced fluorescence. (c) Examples of raw PIV and LIF images and locations of the camera fields of view. The air-side portion of the collated raw PIV image is plotted above the water-side portion of PIV SD image used for surface detection (bottom). Note that, since the LIF cameras are fitted with amber bandpass filters, the green-light-reflecting fog particles are invisible, rendering LIF images ideal for automatic surface detection. All images shown here were acquired nearly at the same instant in time, with time intervals between snapshots less than $30 \mu\text{s}$. No motions of the water surface are detectable (with an image resolution of $100 \mu\text{m}$ per pixel) within that time interval.

(120 mJ per pulse, 3–5-ns pulse duration), with the surface. A similar technique was used by [Duncan et al. \(1999\)](#) to study the surface profiles of mechanically generated breaking waves. The resulting LFV images provided measurements of the along-wind surface elevation in the center line of the channel over a 51.2-cm length (0.25-mm resolution), at a rate of 7.2 Hz.

b. Airflow velocity measurements above waves

The bulk of the data presented in this paper was derived from measurements of two-dimensional (2D) velocity fields in the airflow above the waves. These were

collected using the PIV system described below. Along-channel 2D velocity fields were measured in the air above the middle portion of the LFV wave profiles. The airflow was seeded with 8–12- μm water droplets generated by a commercial fog generator (Microcool, Inc.) equipped with 39 fog nozzles, affixed to an airflow straightener at the location of zero fetch. The Stokes number for the tracer particles was found to be $O(0.01)$, which yielded a root-mean-square (RMS) tracking error below 1% ([Raffel et al. 2007](#)). The particles were illuminated by a high-intensity green laser sheet, generated by a second Nd:YAG laser (200 mJ per pulse, 3–5-ns

TABLE 1. Experimental conditions. Peak wave frequencies f_p were obtained from the WG frequency spectra. Other parameters with subscript p were derived by applying linear wave theory to f_p . Variable a is $\sqrt{(2)a_{\text{rms}}}$, where a_{rms} is the RMS amplitude, computed from the WG time series.

C_p/u_*	C_p/U_{10}	u_* (cm s $^{-1}$)	U_{10} (m s $^{-1}$)	C_p (m s $^{-1}$)	a (cm)	λ_p (m)	ak_p	f_p (Hz)
No waves								
—	—	2.6	0.86	—	—	—	—	—
Wind waves								
1.4	0.06	67.2	16.63	0.92	2.29	0.54	0.27	1.7
1.6	0.06	53.8	14.34	0.87	1.96	0.48	0.26	1.8
2.5	0.08	31.4	9.41	0.78	1.20	0.39	0.19	2.0
3.7	0.12	16.7	5.00	0.62	0.50	0.25	0.13	2.5
6.5	0.22	7.3	2.19	0.47	0.15	0.14	0.07	3.3
Wind over mechanical swell								
6.4	0.23	20.3	5.60	1.30	2.72	1.08	0.16	1.2
7.5	0.25	17.2	5.16	1.30	1.43	1.08	0.08	1.2
16.1	0.52	8.1	2.48	1.30	1.36	1.08	0.08	1.2
18.1	0.56	7.2	2.32	1.30	2.02	1.08	0.12	1.2
19.1	0.57	6.8	2.30	1.30	2.63	1.08	0.15	1.2
25.7	0.83	7.6	2.36	1.95	2.73	2.44	0.07	0.8
27.7	0.93	4.7	1.40	1.30	2.63	1.08	0.15	1.2
31.7	0.97	4.1	1.34	1.30	2.00	1.08	0.12	1.2
38.6	1.39	8.1	2.44	3.12	2.72	6.25	0.03	0.5
47.3	1.45	4.1	1.35	1.95	2.74	2.44	0.07	0.8
66.7	2.15	4.7	1.45	3.12	2.73	6.25	0.03	0.5

pulse duration), and imaged by two side-by-side (2048×2048 pixels, model JAI RM-4200) CCD cameras. The adjacent PIV frames were collated in order to obtain a high-resolution ($47 \mu\text{m}$ per pixel) $18.7 \times 9.7 \text{ cm}$ PIV image, which was then processed with final interrogation windows of 8×8 pixels, with 50% window overlap, yielding 1 velocity vector measurement every $180 \mu\text{m}$. The PIV cameras operated at 14.4 frames per second, yielding PIV velocity estimates at a 7.2-Hz rate. A sample collated PIV image is plotted in Fig. 1c. Secondary laser light reflections near the air–water interface made precise, automated surface detection difficult on the raw PIV images. To address this issue and properly locate the air–water interface on the PIV images, high-resolution ($100 \mu\text{m}$ per pixel) LIF images [PIV surface detection (SD) images] of the wave surface profiles within the PIV field of view were acquired simultaneously with the PIV images, using another CCD camera. Automotive window wipers were placed in front of the cameras inside the flume in order to clean the accumulated fog off the tank windows. Finally, light-scattering material was placed at the bottom of the tank, under the imaging area, in order to avoid intense laser sheet reflections back into the imaging area.

The PIV images were processed using an algorithm based on the adaptive PIV algorithm described in Thomas et al. (2005), which relies on a pyramid cascade of interrogation windows in order to achieve large dynamical range in the velocity. Subpixel resolution was obtained using a three-point Gaussian least squares fit.

The PIV algorithm was run only on the portion of the image that is in the air above the instantaneous water surface. To achieve this, we developed a surface detection algorithm for the PIV SD images based on local variations of image intensity gradients (edge detection) to accurately locate the surface.

c. Coordinate transformation and phase detection

By using the LFV wave profiles, we were able to decompose every PIV water surface into spatial Fourier components and derive a coordinate system that follows the surface near the surface and tends toward a Cartesian coordinate system away from the surface, similar in concept to hybrid coordinate systems used in atmospheric models. Since wind waves contain a number of different Fourier modes, the lines of constant ζ and ξ (see definitions below) also contain several modes. Higher-order modes (large wavenumbers) decay much faster than lower-order modes, which is physically intuitive, in the sense that longer waves perturb the airflow up to a higher altitude than shorter waves do. We introduce curvilinear coordinates (ξ, ζ) related to Cartesian coordinates (x, z) by

$$\xi(x, z) = x - i \sum_n a_n e^{i(k_n \xi + \phi_n)} e^{-k_n \zeta} \quad \text{and} \quad (1)$$

$$\zeta(x, z) = z - \sum_n a_n e^{i(k_n \xi + \phi_n)} e^{-k_n \zeta}, \quad (2)$$

where a_n , k_n , and ϕ_n are respectively the amplitude, wavenumber, and phase of the n th mode in the Fourier decomposition of the water surface $\eta(\xi)$:

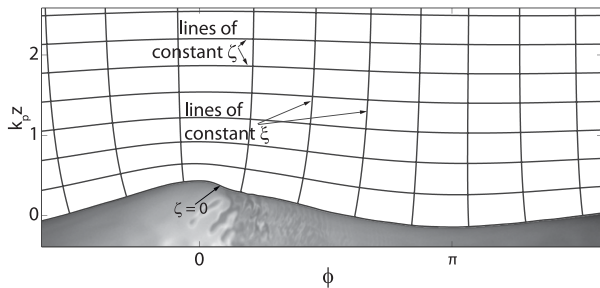


FIG. 2. Sketch of the surface following coordinate transformation used in this study. The ζ coordinate is surface following at the surface and decays toward the Cartesian coordinate z away from the surface; $\zeta = 0$ coincides with the water surface. The ξ coordinate is orthogonal to the surface at the surface and decays toward the Cartesian coordinate x away from the surface. The abscissae are the along-wave phases ϕ .

$$\eta(\xi) = \sum_n a_n e^{i(k_n \xi + \phi_n)}. \quad (3)$$

Only the real parts of Eqs. (1)–(3) are considered. Figure 2 shows a sketch of the decaying surface-following grid. For clarity, only a small fraction of the grid lines are represented. Note that farther away from the surface, high-order modes such as the ripples present on the surface on grid line $\zeta = 0$ decay and disappear first, then the dominant mode decays slowly toward a horizontal line. Such a multimodal curvilinear transformation was first introduced for a wind–wave interaction numerical model by Chalikov (1978). It is worth mentioning here that while this type of coordinate system is now somewhat frequently used in computational studies (e.g., Hara and Sullivan 2015), experimental studies were, until now, not able to report data using such transformations.

Wave phase detection within the PIV field of view was achieved for wind waves by applying a Hilbert transform (Oppenheim and Schafer 2013; Melville 1983) directly to the LFV wave profiles. Further details of this technique applied to surface waves were presented in Hristov et al. (1998). The phases ϕ in the abscissa of

Fig. 2 were obtained using this method. In the case of longer swells, only a fraction of a wavelength was visible on the LFV images (see, e.g., Fig. 5b), rendering any Fourier/Hilbert analysis impossible. Thus, MGR wave phases were detected by computing Hilbert transforms of the WG time series upwind and downwind of the PIV field of view (WG2 and WG3) and linearly interpolating phases between WG2 and WG3 at the times matching with the PIV frame acquisitions.

d. Triple decomposition

To analyze the airflow measurements above the wavy surface, we will use the coordinate system presented above, along with a wave-phase decomposition of the data. A quantity q near the wavy interface can be represented as the sum of a phase-averaged $\langle q \rangle$ and a turbulent perturbation (e.g., Phillips 1977):

$$q(x, z, t) = \langle q \rangle(\xi, \zeta) + q'(x, z, t). \quad (4)$$

Wave phase detection and subsequent conditional averaging (by phase bin) yields $\langle q \rangle$ directly. Turbulent quantities are then simply obtained by subtracting $\langle q \rangle(\phi)$ from instantaneous profiles at phase ϕ . The phase-averaged quantity $\langle q \rangle$ can be further decomposed into the sum of a phase-independent mean \bar{q} and a wave-coherent perturbation \tilde{q} . This leads to the following triple decomposition:

$$q(x, z, t) = \bar{q}(\zeta) + \tilde{q}(\xi, \zeta) + q'(x, z, t). \quad (5)$$

It can be noted that in order to define \bar{q} near the wavy boundary, it is necessary to use a wave-following coordinate system, such as the one defined above. Equation (5) is illustrated in Fig. 3, where an instantaneous horizontal velocity field is decomposed into the sum of a mean velocity profile, a wave-coherent velocity field, and a turbulent velocity field. Of course, the wave-coherent component is obtained from an ensemble conditional phase average of many instantaneous velocity measurements.

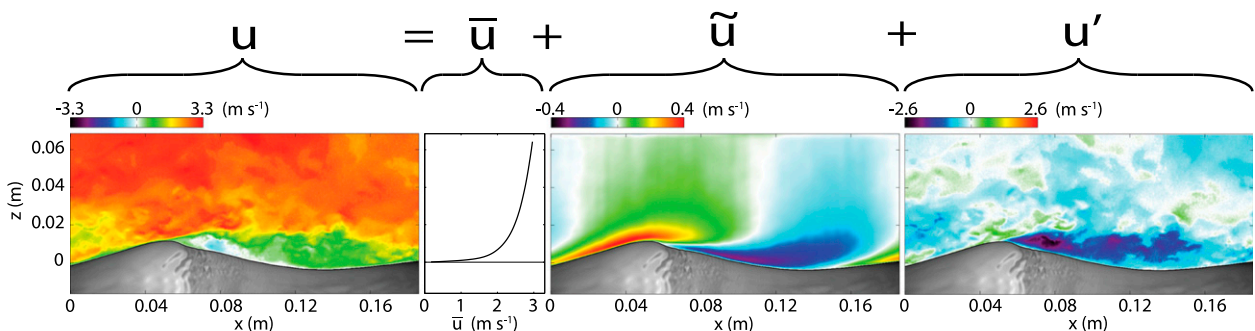


FIG. 3. Example of a triple decomposed instantaneous velocity field [horizontal component $u(x, z, t)$], extracted from the wind wave experiment with $C_p/u_* = 3.7$ ($U_{10} = 5.00 \text{ m s}^{-1}$).

e. Experimental procedure

All devices in the experimental setup described above were controlled by computer, using National Instruments software (LabVIEW) and hardware. The triggers to all six cameras, the two pulsed Nd:YAG lasers, the four WG lasers, and the two window wipers were timed and sent via PCI-6602 timing boards, coupled with BNC-2121 connector blocks. Voltages sent to the wind blower and mechanical wave maker were generated and sampled by a PCIe-6353 data-acquisition board coupled with a BNC-2090A connector block. Each wind wave experiment proceeded as follows: at first, the wind was slowly increased to its target steady value. After the wave field had sufficiently developed and reached a fetch-limited equilibrium state, the fog generator started and the system acquired simultaneously PIV data, LIF PIV SD data, LIF LFV data, and LIF single-point wave height data (WG). The experiments with MGR swells had one additional step: the wave maker was set to generate monochromatic swells throughout the duration of the run. During each experiment, the inside of the tank windows were dried using the window wipers every 30 s, and for a period of 3 s. The images altered by the presence of the wiper were later systematically removed from the dataset. Special attention was given to the placement of the wiper so that it would not interfere with the airflow. All acquired images were transferred to hard drive striped sets by IO Industries frame grabbers. The images were then accessed through IO Industries Streams 5 software, before being processed using MATLAB.

f. Experimental conditions

In this paper, we present results for 17 different wind wave conditions, with wave ages (C_p/u_*) ranging between 1.4 and 66.7. The different experimental conditions are summarized in Table 1. Experiments were performed for durations varying from 4.5 to 14 min, depending on the wind wave conditions. Those durations were calculated based on the estimated dominant wavelength and wave speed for each experiment, with the objective of sampling the same number of waves (approximately 2000) per experiment. During the first experiment ($U_{10} = 0.86 \text{ m s}^{-1}$), the wind did not generate any detectable waves. The mean wind profile above the waveless water surface, obtained from averaging over 2×10^6 profiles obtained by PIV, is plotted in Fig. 4a. The mean wind profile follows the law of the wall, showing clear viscous sublayer, buffer, and logarithmic layers (e.g., Schlichting and Gersten 2000). The fit of the logarithmic part of the mean wind profile is used to estimate values for friction velocity u_* and 10-m extrapolated air velocity U_{10} .

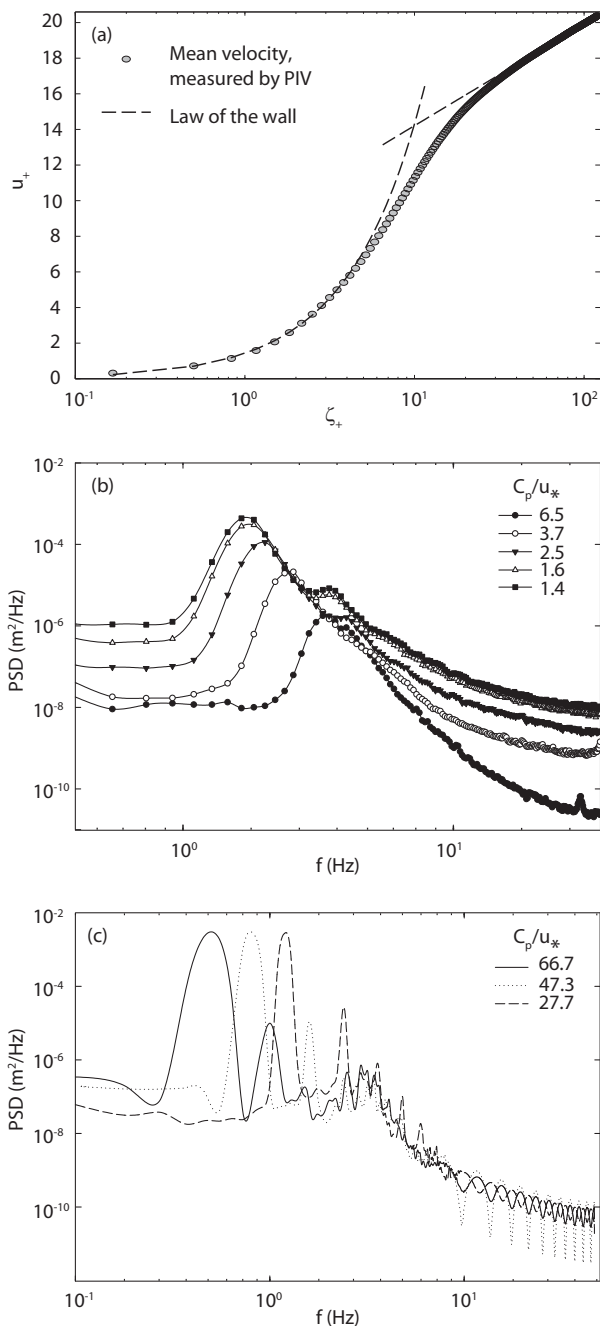


FIG. 4. (a) Mean normalized wind profile from PIV for $U_{10} = 0.86 \text{ m s}^{-1}$ ($u_+ = \bar{u}/u_*$, $\zeta_+ = \zeta u_*/\nu$, with ν the kinematic viscosity of air). Surface-following coordinate ζ is defined in section 2c. Gray circles are data obtained with the PIV, dashed lines are linear and logarithmic fits from the law of the wall. (b) PSDs of water surface elevation time series, measured 1.4 cm upwind of the PIV field of view (WG2) for all wind wave experiments. (c) As in (b), but for three experiments with wind blowing over MGR waves.

Power spectral densities (PSDs) of the water surface elevation were computed from the single-point wave gauge signals. Power spectra for five wind wave experiments are represented in Fig. 4b. The wind wave spectra are relatively narrow banded, with clear peaks at the dominant wave frequency f_p (reported in Table 1). In Fig. 4c, power spectra are shown for three experiments where wind was blowing over MGR waves. The MGR wave spectra show dominant peaks at $f_p = 1.2, 0.8,$ and 0.5 Hz, and a number of sidebands with frequencies that are multiples of f_p . Such harmonics are inevitable in wave-tank mechanical wave experiments (e.g., Bliven et al. 1986). To minimize their presence during the experiments, we limited our mechanical waves to relatively small amplitudes and slopes (see Table 1).

3. Results and discussion

a. Instantaneous turbulent structure of the airflow above waves

In Fig. 5, we show examples of instantaneous 2D velocity fields [horizontal component $u(x, z, t)$, plotted in color] in the air above water, for five different wind wave conditions, plotted above the raw LFV images of the water (water is plotted in gray). The water surface is very different from one experiment to another. No detectable waves are generated by the lowest wind speed $U_{10} = 0.86 \text{ m s}^{-1}$ (Fig. 5a). Old wave age conditions are achieved by blowing similar low winds over MGR swells (Fig. 5b). Only a fraction of a swell wavelength ($\sim 55\%$) is visible here. The wind in this case does not produce any significant waves. At moderate wind speeds, the wind-generated waves are typically nonlinear, with relatively flat troughs and sharp crests, with capillary waves just past the crests (Fig. 5c). The waves steepen with increasing wind speed (Figs. 5d,e), and many entrain air as they break, thereby generating bubbles in the water and spray in the air (not visible here). Also, the water surface becomes covered with small roughness elements [of wavelength $O(1)$ cm]. The grayscale part of the image that is below the water surface is the signature of the underwater part of the LFV laser sheet, refracted through the water surface. These underwater data are difficult to exploit quantitatively but do give a qualitative (albeit distorted) picture of the structure of the surface slope.

1) EJECTIONS AND SWEEPS IN THE AIRFLOW

The turbulent airflow velocity fields above the air-water interface display clear differences from one wind wave condition to another. In Fig. 5a ($U_{10} = 0.86 \text{ m s}^{-1}$),

no waves are being generated, but within the buffer layer, low-velocity fluid is intermittently being ejected away from the water surface and higher-velocity fluid is swept down toward the surface. Such events are also characteristic of the near-wall region in turbulent boundary layers over flat plates, where most of the turbulent stress and kinetic energy throughout the boundary layer are produced [e.g., Kline et al. (1967), and also reviews by Robinson (1991) and Jiménez (2012)]. Later PIV investigations over flat plates (Meinhart and Adrian 1995; Adrian 2007) have also reported ejections or “low momentum ramps” (Jiménez 2012). Ejections (or Q2 events, see below) and sweeps (or Q4 events) have been attributed to hairpin vortices (Adrian 2007) and to quasi-streamwise vorticity streaks in the buffer layer, sweeping and ejecting fluid to and from the boundary (Kim et al. 1971; Robinson 1991; Jiménez 2012). The ejections of low-streamwise-velocity fluid away from the surface cause free shear (spanwise vorticity) layers to form at the interface with the surrounding faster (streamwise) moving fluid. Such high-vorticity layers are directly observed and further discussed below.

In Fig. 5b, where a low wind ($U_{10} = 1.40 \text{ m s}^{-1}$) is blowing over the downwind face of an MGR swell, the ejections appear less intense and more confined to the surface, in spite of the adverse pressure gradient (caused by the presence of the sloping water surface). This is not consistent with the results of Kline et al. (1967) over solid boundaries, who noticed an intensification of ejections in adverse pressure gradient conditions (see also the review by Kovaszny 1970). However, in this case, the near-surface airflow is also strongly influenced by the wave surface orbital motions (see phase-averaged motions in section 3b), which renders the problem more complex and causes important differences from flows over solid boundaries.

2) AIRFLOW SEPARATION EVENTS

The airflow above the wind waves in Figs. 5c–e appears to be separating past the crest of the waves, leading to the formation of a sheltered region of very low (near zero) air velocity downwind of the crest. Airflow separation events were inferred over laboratory wind waves by Chang et al. (1971), Kawai (1981), and Kawamura and Toba (1988), using early flow visualization techniques. Airflow separation over wind waves was later more accurately observed and quantified by Veron et al. (2007) using PIV. However, because of their transient and intermittent nature, separation events within turbulent boundary layers are not easy to define or detect, even over solid boundaries, as was emphasized by Simpson (1989). The conditions for the occurrence of airflow separation over surface gravity waves have been

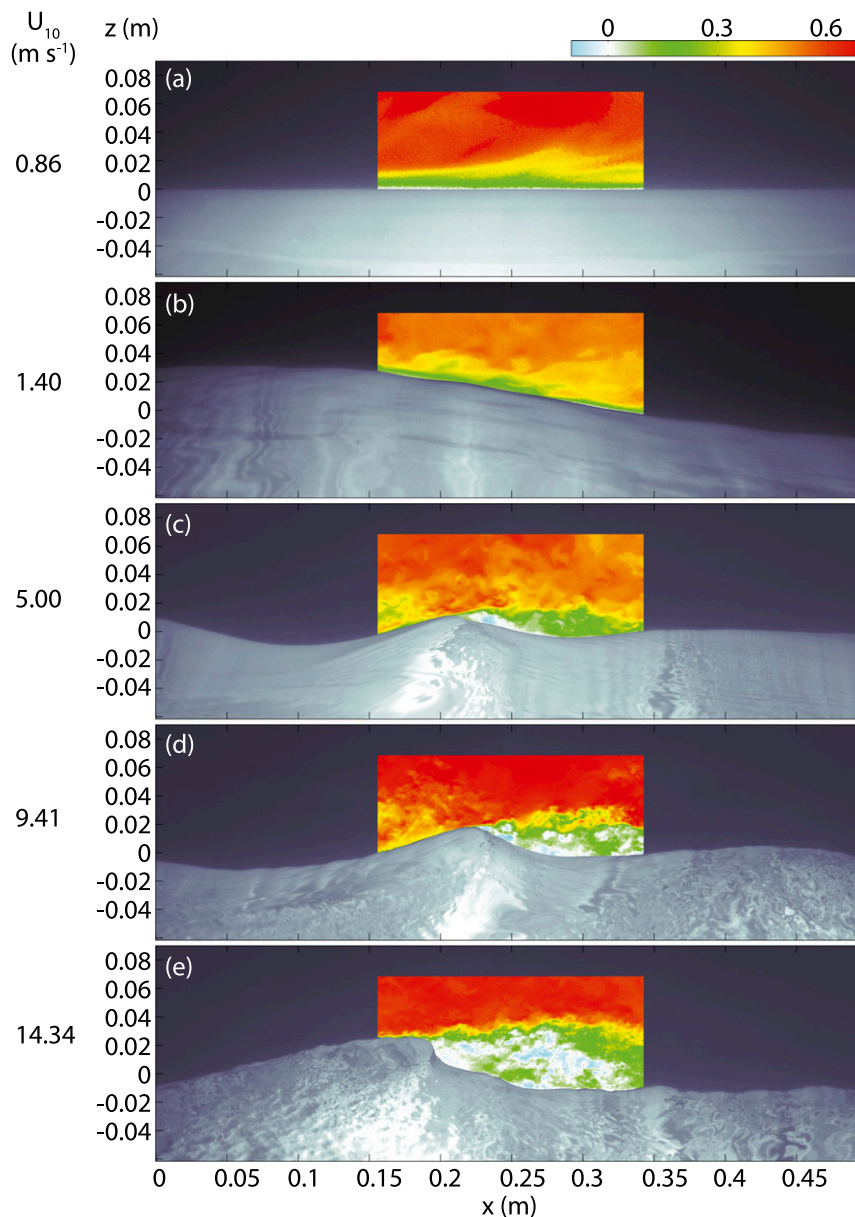


FIG. 5. Examples of instantaneous velocity fields u/U_{10} plotted over LFV images: (a) $U_{10} = 0.86 \text{ m s}^{-1}$, (b) $U_{10} = 1.40 \text{ m s}^{-1}$ with MGR waves, (c) $U_{10} = 5.00 \text{ m s}^{-1}$, (d) $U_{10} = 9.41 \text{ m s}^{-1}$, and (e) $U_{10} = 14.34 \text{ m s}^{-1}$.

the subject of debate, especially since [Banner and Melville \(1976\)](#) and [Gent and Taylor \(1977\)](#) suggested that this may only occur over breaking waves, or in conjunction with strong near-surface underwater drift currents ([Gent and Taylor 1977](#)). Later, [Reul et al. \(1999, 2008\)](#) indeed reported on direct observations of airflow separation past the crest of mechanically generated breaking waves.

[Banner and Melville \(1976\)](#) suggested that separation implies that there is a stagnation point at the surface (in a frame of reference moving with the phase speed of

the wave). In turn, a stagnation point only occurs when the wave is breaking. Their analysis assumes that the wave profile is steady (as is the case, e.g., for linear monochromatic waves in a frame of reference moving with the linear wave phase speed, or for Stokes waves with phase speed $c = \{g/k[1+(ak)^2]\}^{1/2}$). The analysis of [Banner and Melville \(1976\)](#) builds upon the work of [Banner and Phillips \(1974\)](#), who proposed a kinematic criterion for incipient breaking in the presence of a wind drift layer and with similar assumptions on the steadiness of the wave shape.

In the work presented here, while separation is clearly observed, the issue of assessing breaking is delicate. The multimodal nature of the wind waves precludes a steady waveform. In the more narrow-banded MGR swell cases, even though the presence of the wind also generates other wave modes, making the wave shape at best quasi-steady in the frame of reference moving with the swell speed, we do not observe clear separation events and we certainly do not anticipate that these long waves would be breaking. In fact, assuming surface drifts of $q_o = 0.55u_*$ (Wu 1975), only the wind waves at $U_{10} = 16.63 \text{ m s}^{-1}$ and $U_{10} = 14.34 \text{ m s}^{-1}$ are predicted to systematically break, but we note that at lower wind speeds, locally at least, individual wind waves might satisfy Banner and Phillips' (1974) breaking criterion.¹ For the mechanical swell cases, our results are consistent with the analysis of Banner and Melville (1976). For wind waves, besides the kinematic breaking criterion of Banner and Phillips (1974), we have no definitive way to satisfactorily assess breaking. At this point, the present data cannot address, in a definitive manner at least, the potential linkage between airflow separation and surface wave breaking.

The intermittency of airflow separation events above waves adds to the difficulty of obtaining experimental evidence. In this study, we consider that the airflow separates if the near-surface, high-vorticity layer characteristic of an attached boundary layer (Wu et al. 2006; Veron et al. 2007) is ejected away from the water surface and the surface (spanwise) vorticity within the sheltered region is near zero or negative (shown later in Fig. 6). Identifying such events requires high-resolution measurements very close to the surface. The detached high-vorticity layer (due to high shear) may then be a source of intense turbulence farther downwind of the wave crest and away from the water surface.

3) ALONG-WAVE VARIABILITY OF THE INSTANTANEOUS AIRFLOW STRUCTURE

Since the PIV field of view is only a small fraction (approximately 16%) of the wavelength of the MGR swell, Fig. 5 does not show a full picture of the dynamics above all phases of the large MGR waves. To provide a more comprehensive overview, instantaneous fields taken at different times are displayed side by side in

Fig. 6, yielding a picture of the airflow above at least one full wave. The snapshots are taken at intervals of respectively 0.39 s (for $C_p/u_* = 3.7$ and 6.5) and 0.14 s (for $C_p/u_* = 6.4, 19.1,$ and 27.7), with time decreasing from left to right. Over the younger waves ($C_p/u_* = 3.7, 6.4,$ and 6.5), the general pattern is that u increases above crests and decreases above troughs (Figs. 6a1–a3), and w is mostly positive upwind of crests and negative downwind (Figs. 6b1–b3). In addition, low-velocity fluid is ejected away from the surface along the downwind face of the young waves (see, e.g., Figs. 6a2,a3). Over the older waves ($C_p/u_* = 27.7$), the trend is reversed: the airflow very clearly moves downward over the upwind face and upward downwind of the wave crest represented here (Fig. 6b5). In this case, u shows ejections of low-velocity fluid predominantly upstream of the crest (Fig. 6a5). For all wave ages, when u is high near the surface (Fig. 6a), the vorticity is generally high and positive (and due to high shear) at the surface (Fig. 6c), which is characteristic of attached boundary layers (e.g., Wu et al. 2006). When the near-surface velocity u decreases (see, e.g., the downwind face of the waves in Figs. 6a2,a3), near-surface shear is reduced and the surface high vorticity layer may thicken and detach from the surface, as it is less constrained to the surface by the (weaker) velocity gradient (e.g., Figs. 6c2,c3). In the younger wave case ($C_p/u_* = 3.7$), the surface vorticity layer dramatically detaches from the surface past the crest of steep waves, causing airflow separation (Fig. 6c1). At the higher wind speeds, most detached free high-vorticity layers appear to disintegrate and shed a number of small-scale vortices (Figs. 6c1,c2, where $U_{10} = 5.00$ and 5.40 m s^{-1}). At lower wind speeds (Figs. 6c3–c5, $U_{10} = 2.19, 2.30, 1.40 \text{ m s}^{-1}$), we also observe detached high-vorticity layers, but these remain somewhat coherent even away from the surface. It should be noted that the airflow separation that takes place in Fig. 6c1 is not only characterized by a detachment of the surface high-vorticity layer, but also by a total absence of a surface vorticity layer in the sheltered region, which indicates a clear separation of the flow from the boundary (Simpson 1989). In the lower wind speed wind wave case ($U_{10} = 2.19 \text{ m s}^{-1}$, Fig. 6c3), the airflow does not clearly detach from the surface because vorticity does not completely drop at the surface, but one can nonetheless notice that high-vorticity layers (probably due to ejections and sweeps, see above) predominantly originate from the surface just past wave crests, which is coherent with the assumption that they occur more frequently in adverse pressure conditions (Kline et al. 1967; Kovaszny 1970). In this sense, the (albeit very small) waves in Fig. 6c3 are beginning to “organize” the structure of the

¹ We also note that waves are known to break at lower steepnesses than predicted by the kinematic criterion of Banner and Phillips (1974) [see, e.g., the work of Miller et al. (1999) or Yao and Wu (2005)]. Additionally, according to the recent review by Perlin et al. (2013), who summarize the current state of understanding, to date, there are no definitive criteria, whether geometric, kinematic, or dynamic, that can robustly diagnose breaking.

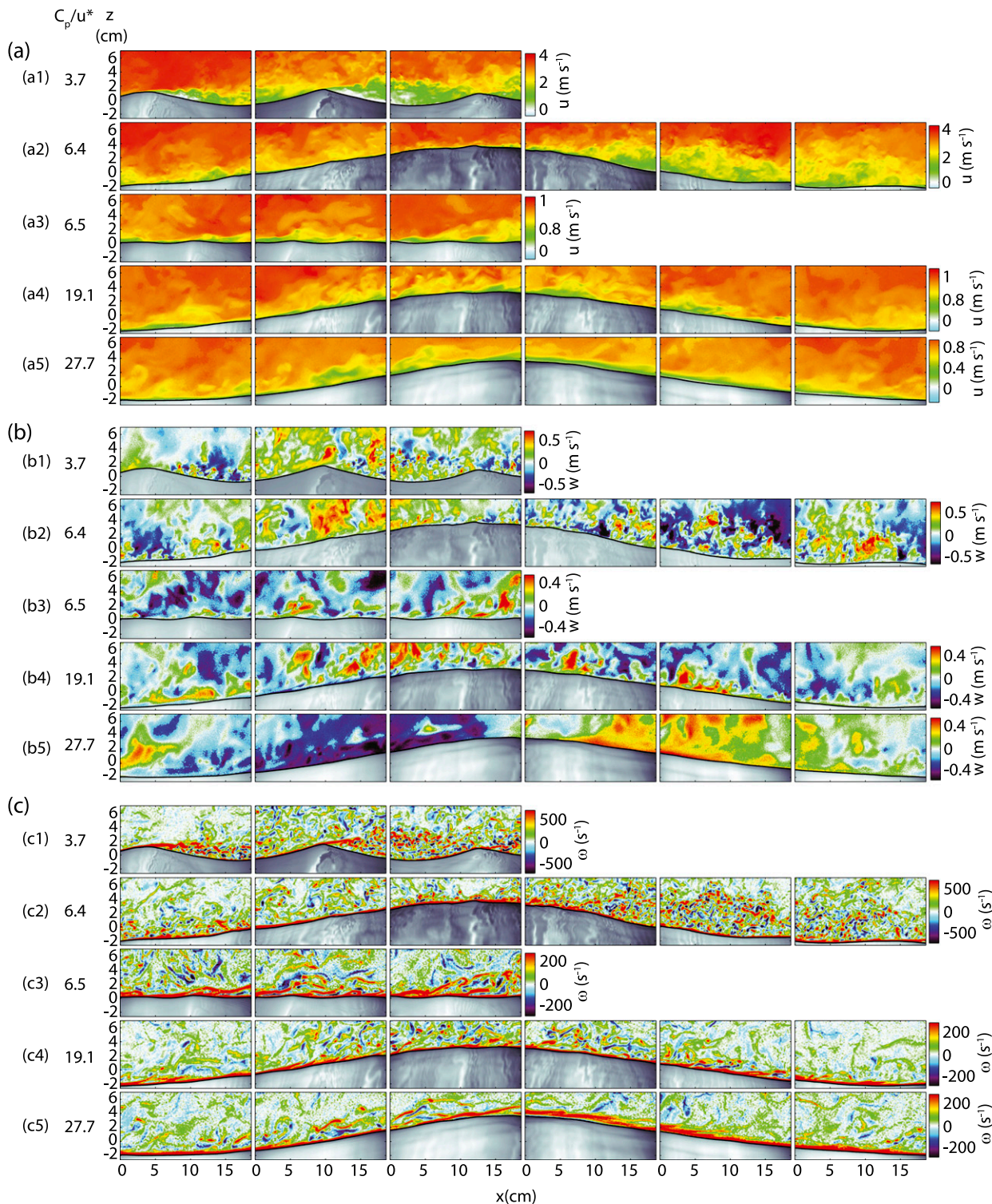


FIG. 6. (a) Instantaneous horizontal velocity fields u (m s^{-1}) above segments of waves. Each row contains consecutive snapshots from one experiment. Mean wave age C_p/u_*^* for each experiment is given on the left. (b) Instantaneous vertical velocity fields w (m s^{-1}). (c) Instantaneous vorticity fields ω (s^{-1}).

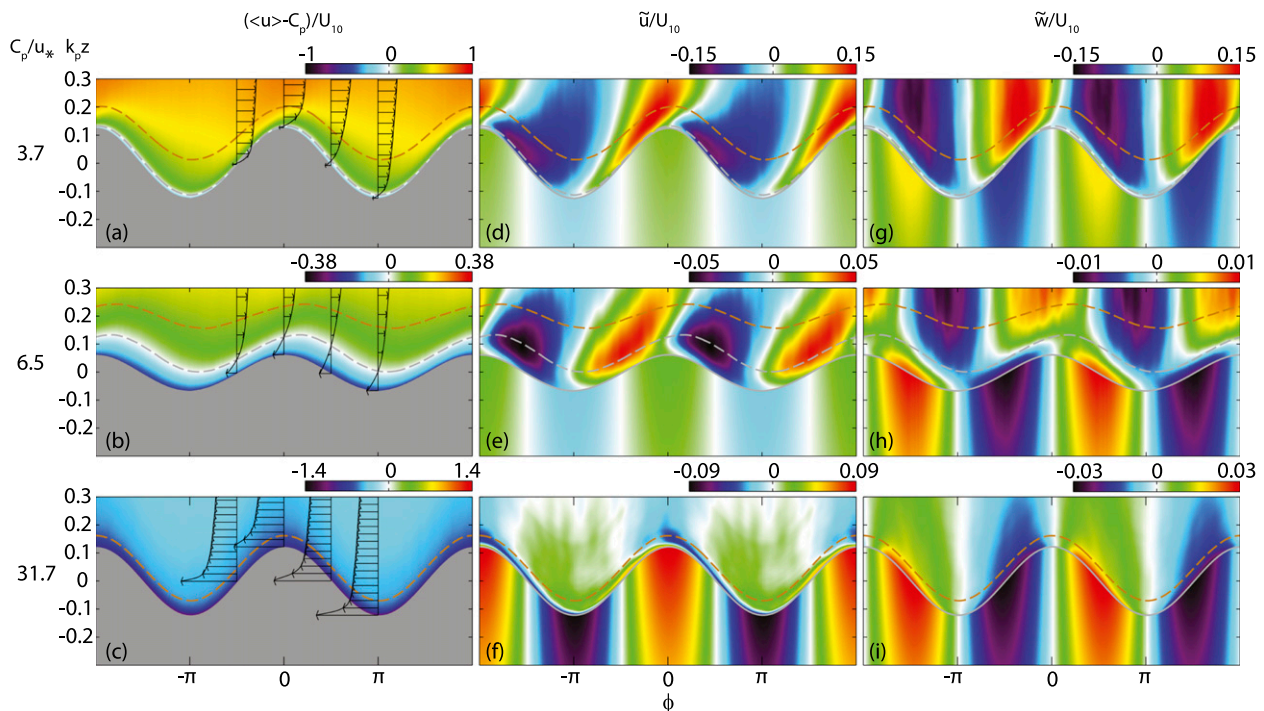


FIG. 7. (a)–(c) Phase-averaged horizontal velocities in the air above waves [$\langle u \rangle - C_p / U_{10}$] in a frame of reference moving at peak phase speed C_p . (d)–(f) Measured wave-coherent horizontal velocities are plotted in the air (\tilde{u} / U_{10}), and the horizontal component of the underwater wave orbital velocities (computed) is plotted below the water surface. (g)–(i) Mean measured vertical velocities \tilde{w} / U_{10} in the air, and vertical underwater orbital velocities. Data in the air are measured; data in the water are computed from linear wave theory. Solid gray lines represent the air–water interface, dashed gray lines show the height of the critical layer ($k_p z_c$), and dashed brown lines represent the top of the inner region ($k_p z_i$) [see Eq. (6)].

turbulence in the airflow, in that the mean characteristics of turbulent quantities will become wave-phase dependent (see averages of turbulent quantities, later in section 3d).

Finally, it is worth noticing that the velocity fields in the air above the younger MGR waves ($C_p / u_* = 6.4$, Figs. 6a2,b2) are (very broadly) “mirror” images of those above the older waves ($C_p / u_* = 27.7$, Figs. 6a5,b5): Fig. 6a2 shows low-velocity fluid ejections downwind of the crest (green and yellow structures extend up to a certain height above the surface), while Fig. 6a5 shows similar structures upwind of the crest. Likewise, w is mostly upward upwind of the crest and downward downwind in Fig. 6b2, while Fig. 6b5 displays the opposite pattern: w downward upwind of crests, and upward downwind. The vorticity fields (Figs. 6c2,c5) yield a similar picture where, in Fig. 6c2, detached vorticity structures are predominantly downwind of the crest, while in Fig. 6c5 they are mostly upwind. These observations hint to a later result in this paper, which is that old waves (here with $C_p / u_* = 27.7$) may cause a “reversed sheltering effect” (see below) or “negative streamline asymmetry” (Belcher and Hunt 1998) near the surface.

b. Phase-averaged velocities

In Fig. 7, we show the phase-averaged velocities in the airflow in a frame of reference moving with the waves at phase speed C_p , for three experiments with different wave ages C_p / u_* . The first two experiments are wind-generated waves (with wave ages $C_p / u_* = 3.7$, and 6.5), and the third is with wind blowing over MGR swell, which allows us to achieve an older wave age of 31.7. The phase-averaged horizontal velocity field $\langle u \rangle - C_p / U_{10}$ shows a phase-locked thickening of the boundary layer² that occurs on average past the crest of the younger waves (Figs. 7a,b). Note that in this frame of reference, the airflow is reversed below the height z_c of the so-called “critical layer” (for the peak waves), defined as the layer of air for which the mean wind speed matches that of the peak wave: $u(z_c) = C_p$ (Miles 1957). The height of the critical layer, the critical height, increases with increasing wave age. In the old wave case ($C_p / u_* = 31.7$), z_c is up to $O(10)$ m, since $U_{10} \sim C_p$. In the youngest

²Also known as “streamline asymmetry” or “sheltering” (Belcher and Hunt 1998).

wave case ($C_p/u_* = 3.7$), the critical height is very small ($\bar{z}_c = 0.6$ mm), with $0.4 \text{ mm} < \langle z_c \rangle < 0.9$ mm. In the older wind wave case ($C_p/u_* = 6.5$), we find $\bar{z}_c = 1.8$ mm, with $1.3 \text{ mm} < \langle z_c \rangle < 2.4$ mm. In both cases, the critical layer follows the undulations of the surface with a lesser amplitude than the surface (especially in Fig. 7b), with a positive phase lag (downstream shift) of approximately $\pi/3$. We emphasize that without the relatively high resolution of the near-surface measurements achieved in this study, the existence of a critical layer over these relatively young wind waves may have been overlooked.

Based on Belcher and Hunt's (1998) approach, we have also estimated the height z_i of the "inner region" (Belcher and Hunt 1993, 1998) above the waves, plotted in dashed brown lines in Fig. 7. Within the inner region (below z_i), Belcher and Hunt (1998) suggested that turbulent eddies are dissipating energy faster than they are distorted by the mean wave-induced strain in the airflow, such that they are in local "equilibrium with the surrounding [near-surface] mean-flow velocity gradient" (Belcher and Hunt 1998). Above z_i , turbulent eddies are subjected to "rapid distortion" (Belcher and Hunt 1998) as they are advected by the mean wave-coherent airflow. Equating estimates of the eddy advection time scale to that of eddy dissipation gives an estimate of the depth of the inner region above waves (Belcher and Hunt 1998; Grare et al. 2013a):

$$k_p z_i |\langle u \rangle(z_i) - C_p| = 2\kappa u_*, \quad (6)$$

where $\kappa = 0.4$ (von Kármán constant). In the two wind wave cases ($C_p/u_* = 3.7$ and 6.5), the critical layer is within the inner region, which is thin upwind of crests and thickens downwind of wave crests. In addition, the inner region is thicker in the older wind wave case ($C_p/u_* = 6.5$) than in the younger wave case ($C_p/u_* = 3.7$). Above the old waves ($C_p/u_* = 31.7$), the situation is different: the thin inner region is slightly thinner downwind of crests and thicker above troughs. This is qualitatively consistent with model results from Cohen and Belcher (1999) over "fast-moving waves" (i.e., old waves; Cohen and Belcher 1999). (This is also clearly visible later in Fig. 9c.)

The wave-coherent (or wave "perturbation"; e.g., Belcher and Hunt 1998) velocities \tilde{u}/U_{10} and \tilde{w}/U_{10} display different patterns below and above the critical layer. Looking at the horizontal wave perturbation velocity first, in Fig. 7d, the streamwise velocities in the air \tilde{u}/U_{10} follow an alternating positive–negative pattern. Near the surface, \tilde{u} is positive on average along the upwind face of waves ($-\pi < \phi < 0$) and negative along the downwind face ($0 < \phi < \pi$). In other words, $\tilde{u}(z \sim \eta)$ is

correlated with the water surface elevation, with a negative phase lag $\phi_{\eta\tilde{u}}$ of approximately $-\pi/2$. However, the magnitude of this phase lag is reduced with increasing height above the water surface and reaches 0 around $k_p z \sim 0.3$, because the velocity contours are tilted downwind, unlike \tilde{w}/U_{10} contours, for example (Fig. 7g), which remain vertical throughout the sampled air column. A similar (downwind tilted) pattern is visible in Fig. 7e, above the critical layer. One would expect such patterns over solid hills. In fact, this sheltering effect was described by Belcher and Hunt (1993, 1998). It was also observed by direct numerical simulation over monochromatic sinusoidal waves and solid hills (Sullivan et al. 2000; Kihara et al. 2007). Below the critical layer, the situation is reversed. The magnitude of the phase lag between \tilde{u} and η increases from the surface to the height of the critical layer, where it is maximum (Figs. 7d,e) and increases with height. Over the older waves in Fig. 7f, the \tilde{u} contours are dramatically tilted upwind very close to the surface, such that the phase lag reaches approximately $-\pi$ at the top of the inner region. In Fig. 7d, since the critical layer is so low, most of the wave perturbation field shows only downwind-tilted velocity contours. Nonetheless, sharp kinks in the velocity contours are visible very close to the surface (e.g., at $\phi = -\pi/2$). Notice that the upwind-tilted positive–negative contours in Fig. 7f can be seen as a mirror image of the downwind-tilted positive–negative patterns in Fig. 7d. At the surface of the old waves (Fig. 7f), the positive (negative) \tilde{u}/U_{10} contours are connected to, and of the same order as, their underwater positive (negative) counterparts. It is important to mention here that the data above the surface are from the PIV measurements while the results below the wave-phase-averaged surface are calculated from linear water–wave theory. It is apparent that the old waves ($C_p/u_* = 31.7$) traveling from left to right are generating, near the surface, a horizontal airflow perturbation reminiscent of a flow traveling in the opposite direction (from right to left). Away from the surface, \tilde{u}/U_{10} is negative above crests and positive above troughs. This pattern is qualitatively coherent with predictions from linear wave theory (inviscid potential flow). However, in our case, the effects of viscosity near the surface modify the classical critical layer theory. These effects are apparent, for example, in Figs. 7d–f.

The vertical wave-coherent velocities \tilde{w}/U_{10} also show two distinct patterns, below and above the critical layer. Below $k_p z_c$, the measured airflow velocities match well with the underwater orbitals, especially for the two older wave cases (Figs. 7h,i). Over the younger waves (Fig. 7g), the matching with underwater orbitals is not as obvious, since the critical layer is so low, although the negative underwater orbitals do appear to have a weak

coupling with the airflow very close to the surface (e.g., over troughs, just past $\phi = \pi$). The fact that this matching only occurs for the (negative) perturbation velocities at that particular phase may be due to the effect of sheltering (separated or not). The sheltering effect causes systematic velocity reduction over troughs, whereby the flow would be “slow” enough with respect to C_p (i.e., the “local wave age” at that phase would be large enough) for the orbitals to influence the airflow. Above the critical height, the alternating negative–positive patterns are dramatically phase-shifted upwind with respect to the underwater patterns. This suggests that at those heights, the airflow is not influenced by the orbitals, but rather by a sheltering effect past the wave form. For $C_p/u_* = 6.5$ (Fig. 7h), the phase lag between \tilde{w} and the surface elevation η , below the critical height, is $\phi_{\eta\tilde{w}} \sim \pi/2$ (with the maximum \tilde{w} on the downwind face of the wave). This phase lag is consistent with potential linear wave theory. Above the critical height, $\phi_{\eta\tilde{w}} \sim 0$. This phase difference $\delta\phi \sim -\pi/2$ across the critical layer is in agreement with the predictions of the critical layer theory (Miles 1957; Davis 1970; Miles 1993) and consistent with the field observations of Hristov et al. (2003) and Grare et al. (2013a). For the younger waves with $C_p/u_* = 3.7$, $\delta\phi \sim -\pi$, also in agreement with the critical layer theory.

c. Wave-induced momentum fluxes

The mean wave-coherent stresses, plotted in Fig. 8, vary dramatically as a function of wave age, wave phase, and height above the water surface. Over the younger waves (Fig. 8a), the phase-averaged wave-coherent stress $-\langle \tilde{u}\tilde{w} \rangle / u_*^2$ is intense and negative upwind of crests, and slightly less intense and negative downwind of crests. It can be noted here that this asymmetry in the negative wave stress intensities above the critical height is reminiscent of the asymmetry caused by the sheltering effect in the phase-averaged horizontal velocities [$(\langle u \rangle - C_p)/U_{10}$] above the critical height (previously observed in Figs. 7a,b). The large (and downwind tilted) jets of negative flux are interlaced with narrower less intense positive flux contours. These are tilted downwind above crests and are nearly vertical (no tilt) above troughs, just past $\phi = \pi$. This is also the phase at which the negative surface orbitals are able to “draw” the airflow downward (Fig. 7g), as suggested in section 3b. The overall pattern of $-\langle \tilde{u}\tilde{w} \rangle / u_*^2$ above these slow, young wind waves is not specific to moving water waves; it is presumably also present when sheltering occurs over a solid wavy boundary (Sullivan et al. 2000).

Over the slightly older wind waves (Fig. 8b), broadly similar sheltering patterns in the wave stress are also present (also asymmetrical in intensity), but only above

the critical layer. The regions of intense negative stress in the airflow above the critical height, are located at phases where the underwater orbital stress is positive. At the surface, they are (weakly) connected to regions of negative underwater orbital stresses, at phases $\phi = \pm\pi$ (see also Fig. 9b below). In contrast, near the surface, below the critical height, contours of intense positive flux dominate and cover nearly the entire upwind and downwind faces of the waves. These contours are tilted upwind, and while they are more intense than the underwater stresses, they appear nonetheless to be continuous across the air–water interface (and match the theoretical underwater estimates) just before crests and just before troughs ($-\pi/2 < \phi < 0$ and $\pi/2 < \phi < \pi$). These regions of positive wave stress are predominantly located under the critical height, while the regions of negative stress dominate above $k_p z_c$. It should also be noted that the regions of positive wave stress are more intense along downwind wave faces than along upwind faces; in other words, the wave stress below the critical layer presents a pattern of negative asymmetry.

Over the older MGR waves (Fig. 8c), $-\langle \tilde{u}\tilde{w} \rangle / u_*^2$ patterns resemble those in the oldest wind wave case above (Fig. 8b), except that the positive stress regions are very intense (with magnitudes nearly 8 times the total kinematic stress u_*^2) and very thin, and the negative stress regions are comparatively very weak (with magnitudes approximately 10% of the thin positive stress regions). It is important to notice here that in the case of these older waves ($C_p/u_* = 31.7$), the shift from positive near-surface wave stresses to largely negative stresses takes place at the top of the inner region.

In the two wind wave cases (Figs. 8d,e), the mean normalized wave stress $-\langle \tilde{u}\tilde{w} \rangle / u_*^2$ is positive below the critical layer and negative above. This is in agreement with results from Hsu et al. (1981), Sullivan et al. (2000), and Yang and Shen (2010). Over the younger steeper waves ($C_p/u_* = 3.7$), the mean negative wave stress represents over 60% of the total kinematic stress u_*^2 , at $k_p \zeta = 0.08$ (Fig. 8d). The near-surface positive wave stress below the very small critical height is comparatively very small (less than 1% of the total stress). Over the wind waves with $C_p/u_* = 6.5$, the mean positive (negative) wave stress reaches roughly 10% of the total stress below (above) the critical layer (Fig. 8e). Over the old mechanical waves ($C_p/u_* = 31.7$), the near-surface positive flux reaches extreme values (on average 300% of the total stress). The mean stress becomes negative away from the surface, at the top of the inner region. Similar results were found by Sullivan et al. (2000) by direct numerical simulation over monochromatic waves $(C_p/u_*, ak) = (22.7, 0.1)$. They obtained a near-surface positive momentum flux that reached just over 100% of the total stress, and a

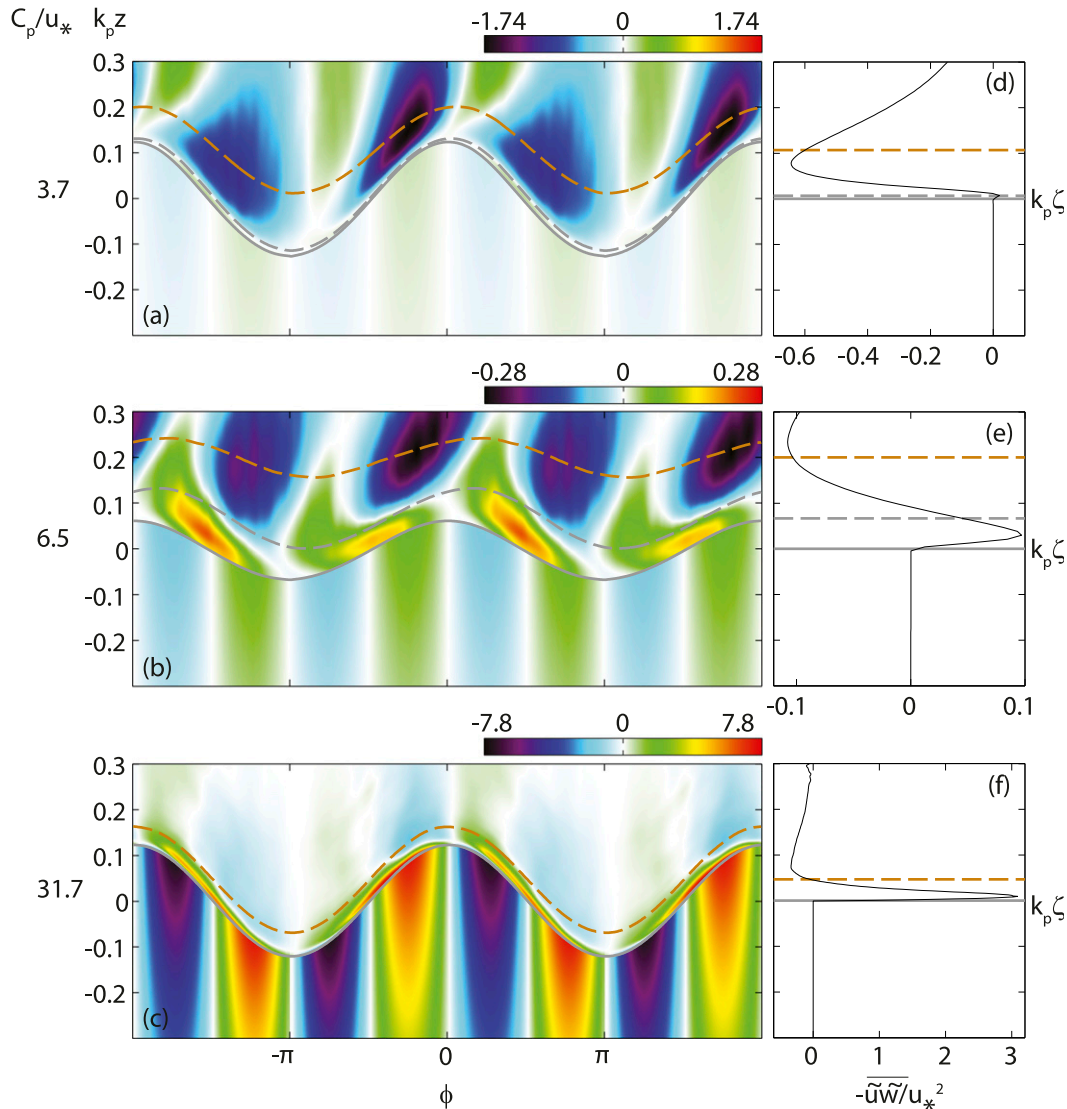


FIG. 8. (a)–(c) Normalized phase-averaged wave stress $-\langle \tilde{u}\tilde{w} \rangle / u_*^2$. (d)–(f) Total mean (for all phases) wave stress $-\bar{u}\bar{w} / u_*^2$. Phase averages are plotted above the phase-averaged water surface elevation, and total mean profiles are plotted with respect to the surface following vertical coordinate $k_p \zeta$. Each row corresponds to one experiment, and the corresponding wave ages are indicated on the left. Data in the air are measured; data in the water are computed from linear wave theory.

slightly negative overshoot above. Our MGR waves are older and slightly steeper $(C_p/u_*, ak) = (31.7, 0.12)$; this could partially explain our larger values.

These observations suggest that over young wind waves $(C_p/u_* < 3.7)$ the wave form is forcing on average a negative wave-perturbation stress. Over slightly older waves (e.g., when $C_p/u_* = 6.5$), the underwater orbitals, of the same order of magnitude as the airflow velocities near the surface, force on average a positive wave-perturbation stress below the critical layer. Above the critical layer, the wave form sheltering effect remains dominant. So in this case, the critical layer

is, for the outer flow, acting as a surrogate slow, young wave, or solid wave form. Over old waves (e.g., when $C_p/u_* = 31.7$), near the surface a reversed wave form sheltering effect takes place. Away from the surface, the wave-perturbation stresses mirror the underwater orbital stresses in qualitative agreement with linear theory.

The very thin regions below the critical height (for the wind waves) and within the inner region (for the old MGR waves) appear to play an important role for the wave-induced momentum flux. To better understand the wave flux patterns within these regions, we have plotted in Fig. 9 the measured air-side fluxes with respect to the

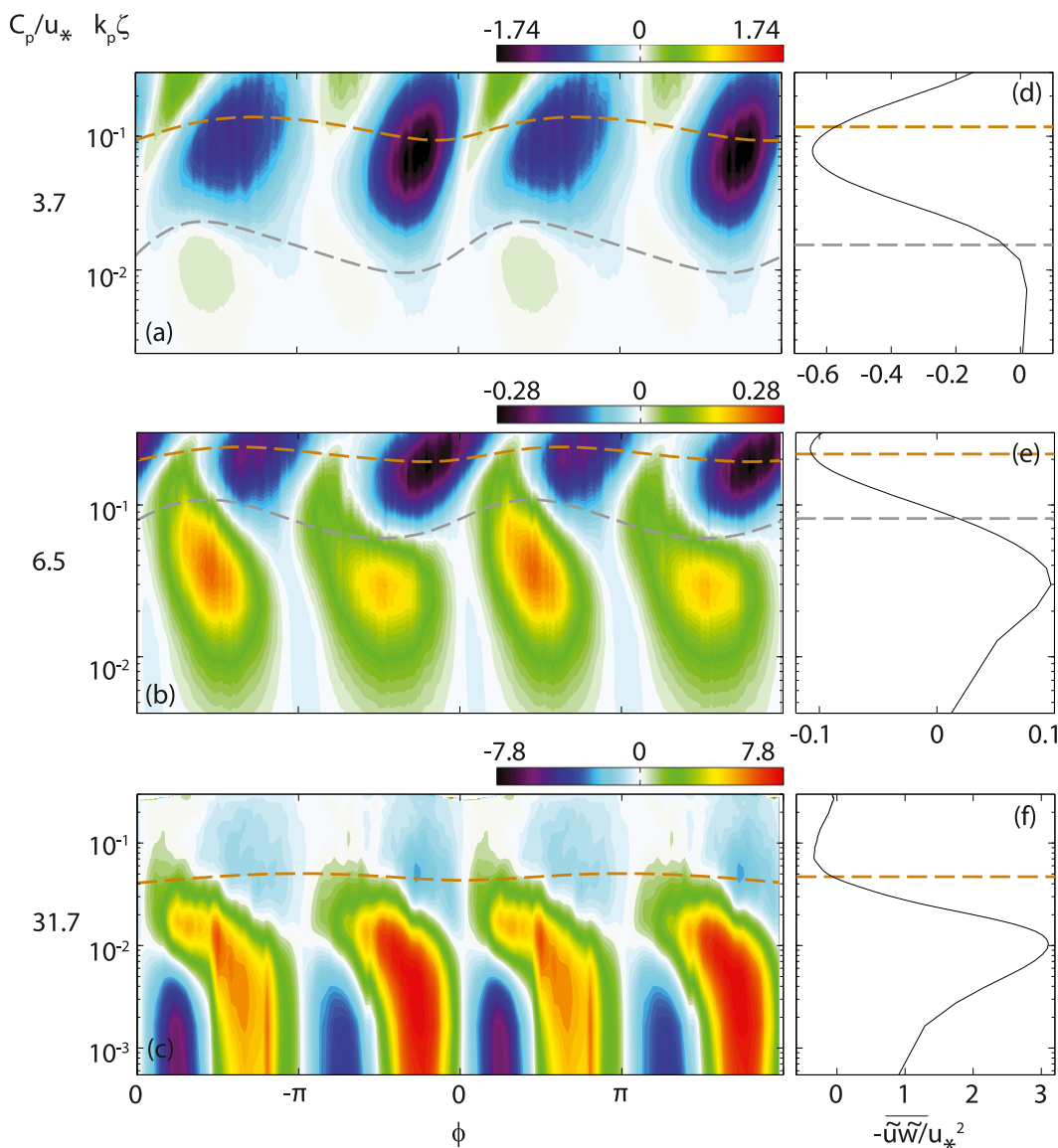


FIG. 9. (a)–(c) Normalized phase-averaged air-side wave stress $-\langle \tilde{u}\tilde{w} \rangle / u_*^2$. (d)–(f) Total mean (for all phases) air-side wave stress $-\overline{\tilde{u}\tilde{w}} / u_*^2$. Both phase averages and total mean profiles are plotted with respect to the surface following vertical coordinate $k_p \zeta$. Each row corresponds to one experiment, and the corresponding wave ages are indicated on the left.

surface following vertical coordinate $k_p \zeta$, with a logarithmic vertical axis. Here, in Fig. 9a, over young wind waves with $C_p/u_* = 3.7$, we can now observe contours of positive wave stresses very close to the surface below the critical height. But these are only visible where the critical height is largest: downwind of wave crests ($\phi \sim \pi/3$). Thus, below the critical height of these young wind waves ($C_p/u_* = 3.7$), we observe a pattern of negative asymmetry in the wave stress. A similar negative asymmetry in positive wave stress was already visible below the critical height above the older wind waves in Fig. 8b (also very clear here in Fig. 9b). Here, in Fig. 9b, we also observe

that the near-surface positive stress contours are interlaced by very weak negative stress contours.

Above the older MGR waves (Fig. 9c), $-\langle \tilde{u}\tilde{w} \rangle / u_*^2$ contours are similar to the ones over the wind waves in Fig. 9b, except here the top of the inner region plays the same role as the critical height does in the younger wind wave case. Above the older waves (Fig. 9c), both positive and negative stress contours are very intense around crests (near $\phi \sim -\pi/4$ and $\phi \sim \pi/4$, respectively) and less intense around troughs (near $\phi \sim 3\pi/4$ and $\phi \sim -3\pi/4$, respectively). This asymmetry is probably caused by a sheltering effect in the upwind direction.

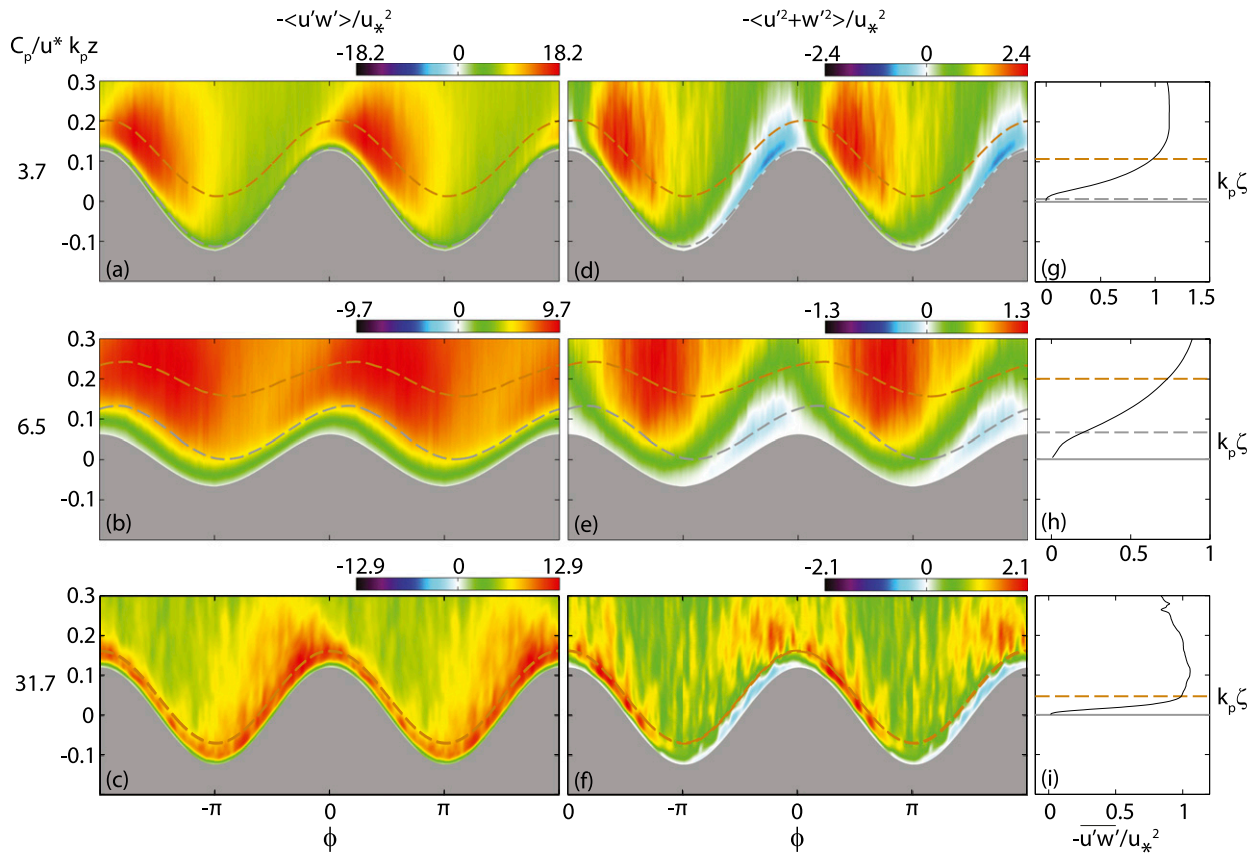


FIG. 10. (a)–(c) Normalized phase-averaged sum of turbulent variance $\langle u'^2 + w'^2 \rangle / u_*^2$. (d)–(f) Normalized phase-averaged turbulent stress $-\langle u'w' \rangle / u_*^2$. (g)–(i) Total mean (for all phases) turbulent stress $-\langle u'w' \rangle / u_*^2$. Phase averages are plotted above the phase-averaged water surface elevation, and total mean profiles are plotted with respect to the surface following vertical coordinate $k_p \zeta$. Each row corresponds to one experiment, and the corresponding wave ages are indicated on the left.

d. Turbulent variances and fluxes

The phase-averaged sum of horizontal and vertical turbulent variances $\langle u'^2 + w'^2 \rangle / u_*^2$ is plotted in Figs. 10a–c, for the same experiments as in sections 3b and 3c. In Fig. 10a, there is a phase-locked jet of intense turbulence past the crest of the waves, away from the surface. We attribute this to airflow separation, whereby high shear layers intermittently detach from the crest of steep waves. Detached (from the surface) free shear layers are sources of intense turbulence away from the surface. Examples of these layers are represented in Fig. 6c. It is worth mentioning that although airflow separation only occurs over a fraction³ (under 20%) of all the waves used to compute the phase-averaged field in Fig. 10a ($C_p/u_* = 3.7$, $U_{10} = 5.00 \text{ m s}^{-1}$), the turbulence generated

by these sporadic events is sufficiently intense to dominate the average. Flow separation past solid periodic hills has been found to generate an average intensification of the turbulent kinetic energy away from the surface downstream of the hill (see, e.g., Breuer et al. 2009). Over the older wind waves ($C_p/u_* = 6.5$), $\langle u'^2 + w'^2 \rangle / u_*^2$ is also intensified downwind of crests and away from the surface (Fig. 10b), but this process is not nearly as pronounced as for the youngest wind waves (Fig. 10a). Also, above the critical layer of the older wind waves, the background turbulence remains relatively high. These observations can be better understood by looking again at Fig. 6c3. There are a number of detached high spanwise vorticity layers (negative and positive) present up to some distance (up to approximately 3 cm) away from the surface above most of the section of water surface plotted here. These are probably sources of turbulence at all phases. Note that Fig. 10b is only showing the turbulence within the first 6.7 mm ($k_p z < 0.3$), where thick (and detached) high vorticity layers are ubiquitous.

³ Separation events were detected automatically using criteria on the near-surface viscous shear and vorticity in the air. Further results will be presented in a subsequent publication and will explore this in more detail.

The older MGR waves cause, on average, an intensification of the turbulence on the windward side of the waves (Fig. 10c). This pattern is (broadly) a reversed picture of what happens above the critical layer over wind waves (Figs. 10a,b). Again, Fig. 6 may shed some light on this phenomenon, specifically in Fig. 6c5, where high-vorticity layers appear to be ejected from the surface on the upwind face of the waves. This is to be expected since these waves travel faster than the wind and are presumably generating a turbulent wake as they propagate.

The distribution of turbulent stress $-\langle u'w' \rangle / u_*^2$ in the airflow is on average also strongly coupled with the waves (see Figs. 10d–f). In all three experiments presented here, the turbulent stress is negative (upward) along the upwind face of the waves and positive (downward) over the downwind face of the waves. Overall, these results support the suggestion by Belcher and Hunt (1993) that the turbulent stresses systematically accelerate the mean flow (upward stress) before the crest and decelerate it (downward stress) past the crest. Over the older MGR waves (Fig. 10f), however, the positive stress region does not remain confined to the leeward side of the waves, but rather extends to the upwind face of the waves (up to $\phi \sim -2\pi/3$) and away from the surface. This effect can be related to the boundary layer thickening (flow deceleration) observed above and slightly upstream of crests in Fig. 7c. The vertical profiles plotted in Figs. 10g and 10i show that the turbulent flux $-\overline{u'w'}$ is $O(u_*^2)$ at the top of the inner region over the youngest and oldest waves (Figs. 10g,i). Above the wind waves with $C_p/u_* = 6.5$, the mean turbulent momentum flux does not reach the level of the total flux until $k_p\zeta = 0.6$ (not shown here).

A quadrant analysis of the turbulent momentum fluxes is presented in Fig. 11, where we have plotted our laboratory results alongside results reported in Sullivan et al. (2008). Quadrant analysis was first introduced by Wallace et al. (1972) and Willmarth and Lu (1972) as a method to understand and quantify turbulent stress-producing motions in solid-wall bounded turbulent boundary layers. Later, the method was applied to turbulent flux measurements within the marine atmospheric boundary layer (Chambers and Antonia 1981; Smedman et al. 1999; Sullivan et al. 2008). Briefly, the ratio $Q_r = -(Q2 + Q4)/(Q1 + Q3)$ represents the importance of downward ($Q2 + Q4 = \overline{u'w'}$, with u' and w' of opposite signs) versus upward ($Q1 + Q3 = \overline{u'w'}$, with u' and w' of same sign) turbulent momentum flux events. Ejections (Q2) and sweeps (Q4) are considered to be the principal mechanisms for downward momentum flux events in turbulent boundary layers. They are also important for the total production of turbulence within

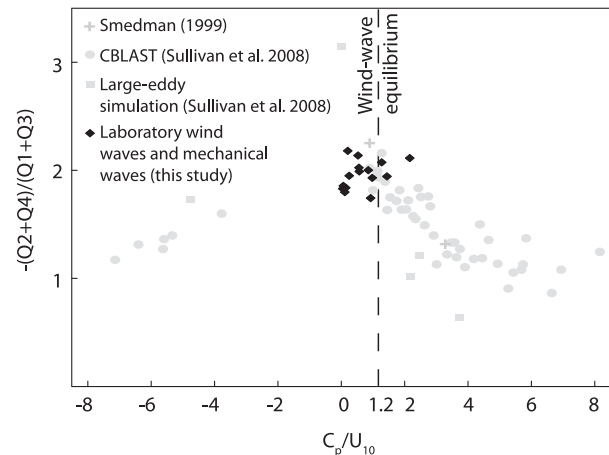


FIG. 11. Quadrant analysis of turbulent momentum flux events, as a function of wave age, $(C_p/U_{10})\cos\alpha$, where α is the angle between wave propagation direction and surface wind (Sullivan et al. 2008). The ratio $-(Q2 + Q4)/(Q1 + Q3)$ represents the importance of downward turbulent momentum flux events ($Q2 + Q4 = \overline{u'w'}$, with u' and w' of opposite signs) vs upward events ($Q1 + Q3 = \overline{u'w'}$, with u' and w' of same sign). Additional data, extracted from Sullivan et al. (2008, their Fig. 16), are provided for comparison with our laboratory results.

turbulent boundary layers (Robinson 1991; Jiménez 2012). Our results, achieved for 10-m wave ages C_p/U_{10} ranging from 0.07 to 2.15, fall well within the results from LES calculations (Sullivan et al. 2008) and field measurements from Smedman et al. (1999) and CBLAST (Edson et al. 2007). Our measurements of turbulent fluxes were taken between $\zeta = 1$ cm and $\zeta = 4$ cm. The downward turbulent flux events are in general twice as important as upward events, which appears to be the norm for waves near the wind wave equilibrium ($C_p/U_{10} = 1.2$; see Alves et al. 2003) such as ours.

4. Concluding remarks

Using an innovative complex imaging system, we were able to obtain high-resolution, two-dimensional velocity measurements in the airflow above waves in the laboratory in a wide range of wind and wave conditions. Our measurements, achieved down to $100\ \mu\text{m}$ from the air-water interface on average, have yielded important results on the turbulent structure of the airflow above waves. Also, using wave-phase sensitive averaging, we were able to estimate the statistical significance of the observed instantaneous structures and understand the impacts of their coupling with the wave field. This was made possible by combining our air-side velocity data with local and surrounding spatial and temporal wave measurements, which allowed us to sort all our data (above short wind waves and above long MGR swells) according to wave phase. We were then able to estimate

phase-averaged velocities and wave-coherent and turbulent momentum fluxes in a wave-following coordinate system.

a. Influence of waves on turbulence in the airflow

The airflow above the waves displays a number of features characteristic of a turbulent boundary layer over a flat plate, such as turbulent ejections away from the interface of low-velocity fluid and high-vorticity layers. These intermittent ejections may in turn impact the distribution of turbulent stress (shear but also pressure driven) along the surface, and thus be an important factor in the initial stages of wind wave generation through turbulent near-surface pressure variations (Phillips 1957; Lin et al. 2008). Once waves are generated, their presence influences the intensity and spatial distribution of these structures along the water surface, which in turn may impact the turbulent boundary layer as a whole. In particular, high-vorticity layers are ejected from the crests of wind waves starting at low wind speeds ($U_{10} = 2.19 \text{ m s}^{-1}$), and airflow separation intermittently occurs past wind waves when $U_{10} = 5.00 \text{ m s}^{-1}$ and $C_p/u_* = 3.7$. The intermittent occurrence of airflow separation past young wave crests dramatically increases the average intensity of the turbulence past crests, produced by detached free shear layers. The role of the inner region for the phase-locked turbulence is unclear. As suggested by Grare et al. (2013a), it may be useful to estimate the thickness of the inner region based on ratios of TKE advection and TKE dissipation, rather than time-scale arguments. Questions also remain as to the coupling of airflow separation events with the motion in the water below, and specifically whether wave breaking is the only condition for the separation of turbulent boundary layers over waves. Simultaneous air and water measurements, using similar high-resolution, two-dimensional techniques as those presented here, would shed some light on this debate. A quadrant analysis of the near-surface turbulent stresses shows trends of predominantly downward turbulent momentum flux events in all our wind wave conditions, which is in agreement with CBLAST field measurements and LES results (Sullivan et al. 2008).

b. Influence of wave age on mean wave-coherent motions and momentum flux

All measured quantities show a strong dependence on the wave phase and the wave age. Very young waves ($C_p/u_* < 4$) were found to have very low critical layers, with on average a large sheltering effect past the crest, where turbulence and turbulent shear stress are very large compared with the surrounding fluid. The height of the critical layer z_c increases with increasing wave age. Over slightly older wind waves ($C_p/u_* = 6.5$), the mean

airflow below the critical layer starts to display a reversed asymmetry (or negative asymmetry; Belcher and Hunt 1998) with respect to the airflow above the critical layer. Vertical wave-perturbation fields show a strong coupling of the near-surface airflow with the underwater motions. Their horizontal counterparts confirm this coupling, but also show the importance of the negative asymmetry effect very close to the surface. These results may point to the importance on average of a critical layer mechanism with viscous effects (Miles 1959) for the growth of young wind waves, in spite of the turbulent nature of the airflow and in spite of the numerous turbulent ejections of high-vorticity structures that leave the surface and cross the critical height. The question of the reduction of turbulent stress by waves in favor of an increased wave-induced stress is not obvious and requires a thorough study of the momentum balance throughout the air above the waves. This entails careful curvilinear projections of the different quantities and appropriate coordinate transformation (Hara and Sullivan 2015) and will be the object of a future study. Above fast (old) waves, the sheltering effect is reversed and is strong within the inner region, and surface orbital velocities appear to strongly influence the airflow throughout the entire air-side boundary layer. Finally, phase-averaged wave-coherent momentum fluxes suggest that the critical layer plays a role in the wind-wave coupling in the two youngest wave cases ($C_p/u_* = 3.7, 6.5$), while the inner region is important for the older waves ($C_p/u_* = 31.7$). These results are in agreement with Belcher and Hunt (1998), Sullivan et al. (2000), Kihara et al. (2007), and Grare et al. (2013a).

Acknowledgments. We sincerely thank Laurent Grare for his comments on an early draft of this paper. We also thank the anonymous reviewers, whose comments and suggestions helped clarify the presentation of this paper. This work was supported by grants OCE-1458977, OCE-1233808, OCE 0748767, and AGS-PRF-1524733 from the National Science Foundation (NSF).

REFERENCES

- Adrian, R. J., 2007: Hairpin vortex organization in wall turbulence. *Phys. Fluids*, **19**, 041301, doi:10.1063/1.2717527.
- Alves, J. H. G., M. L. Banner, and I. R. Young, 2003: Revisiting the Pierson–Moskowitz asymptotic limits for fully developed wind waves. *J. Phys. Oceanogr.*, **33**, 1301–1323, doi:10.1175/1520-0485(2003)033<1301:RTPALF>2.0.CO;2.
- Banner, M. L., 1990: The influence of wave breaking on the surface pressure distribution in wind-wave interactions. *J. Fluid Mech.*, **211**, 463–495, doi:10.1017/S0022112090001653.
- , and O. Phillips, 1974: On the incipient breaking of small scale waves. *J. Fluid Mech.*, **65**, 647–656, doi:10.1017/S0022112074001583.

- , and W. K. Melville, 1976: On the separation of air flow over water waves. *J. Fluid Mech.*, **77**, 825–842, doi:10.1017/S0022112076002905.
- , and W. L. Peirson, 1998: Tangential stress beneath wind-driven air-water interfaces. *J. Fluid Mech.*, **364**, 115–145, doi:10.1017/S0022112098001128.
- Batchelor, G., and I. Proudman, 1954: The effect of rapid distortion of a fluid in turbulent motion. *Quart. J. Mech. Appl. Math.*, **7**, 83–103, doi:10.1093/qjmam/7.1.83.
- Belcher, S. E., and J. C. R. Hunt, 1993: Turbulent shear flow over slowly moving waves. *J. Fluid Mech.*, **251**, 109–148, doi:10.1017/S0022112093003350.
- , and —, 1998: Turbulent flow over hills and waves. *Annu. Rev. Fluid Mech.*, **30**, 507–538, doi:10.1146/annurev.fluid.30.1.507.
- Bliven, L., N. Huang, and S. Long, 1986: Experimental study of the influence of wind on Benjamin-Feir sideband instability. *J. Fluid Mech.*, **162**, 237–260, doi:10.1017/S0022112086002033.
- Breivik, Ø., K. Mogensén, J.-R. Bidlot, M. A. Balmaseda, and P. A. Janssen, 2015: Surface wave effects in the NEMO ocean model: Forced and coupled experiments. *J. Geophys. Res. Oceans*, **120**, 2973–2992, doi:10.1002/2014JC010565.
- Breuer, M., N. Peller, C. Rapp, and M. Manhart, 2009: Flow over periodic hills-numerical and experimental study in a wide range of Reynolds numbers. *Comput. Fluids*, **38**, 433–457, doi:10.1016/j.compfluid.2008.05.002.
- Chalikov, D. V., 1978: The numerical simulation of wind-wave interaction. *J. Fluid Mech.*, **87**, 561–582, doi:10.1017/S0022112078001767.
- Chambers, A. J., and R. A. Antonia, 1981: Wave-induced effect on the Reynolds shear stress and heat flux in the marine surface layer. *J. Phys. Oceanogr.*, **11**, 116–121, doi:10.1175/1520-0485(1981)011<0116:WIEOTR>2.0.CO;2.
- Chang, P. C., E. J. Plate, and G. M. Hidy, 1971: Turbulent air flow over the dominant component of wind-generated water waves. *J. Fluid Mech.*, **47**, 183–208, doi:10.1017/S0022112071001009.
- Chen, S. S., W. Zhao, M. A. Donelan, and H. L. Tolman, 2013: Directional wind-wave coupling in fully coupled atmosphere-wave-ocean models: Results from CBLAST-hurricane. *J. Atmos. Sci.*, **70**, 3198–3215, doi:10.1175/JAS-D-12-0157.1.
- Cohen, J., and S. Belcher, 1999: Turbulent shear flow over fast-moving waves. *J. Fluid Mech.*, **386**, 345–371, doi:10.1017/S0022112099004383.
- Csanady, G. T., 2001: *Air-Sea Interaction: Laws and Mechanisms*. Cambridge University Press, 248 pp.
- Davis, R. E., 1970: On the turbulent flow over a wavy boundary. *J. Fluid Mech.*, **42**, 721–731, doi:10.1017/S002211207000157X.
- Donelan, M. A., F. W. Dobson, S. D. Smith, and R. J. Anderson, 1995: Reply. *J. Phys. Oceanogr.*, **25**, 1908–1909, doi:10.1175/1520-0485(1995)025<1908:R>2.0.CO;2.
- Duncan, J., H. Qiao, V. Philomin, and A. Wenz, 1999: Gentle spilling breakers: Crest profile evolution. *J. Fluid Mech.*, **379**, 191–222, doi:10.1017/S0022112098003152.
- Edson, J. B., and Coauthors, 2007: The Coupled Boundary Layers and Air-Sea Transfer experiment in low winds. *Bull. Amer. Meteor. Soc.*, **88**, 341–356, doi:10.1175/BAMS-88-3-341.
- , and Coauthors, 2013: On the exchange of momentum over the open ocean. *J. Phys. Oceanogr.*, **43**, 1589–1610, doi:10.1175/JPO-D-12-0173.1.
- Gent, P. R., and P. A. Taylor, 1977: A note on separation over short wind waves. *Bound.-Layer Meteor.*, **11**, 65–87, doi:10.1007/BF00221825.
- Grachev, A., and C. Fairall, 2001: Upward momentum transfer in the marine boundary layer. *J. Phys. Oceanogr.*, **31**, 1698–1711, doi:10.1175/1520-0485(2001)031<1698:UMTITM>2.0.CO;2.
- Grare, L., L. Lenain, and W. K. Melville, 2013a: Wave-coherent airflow and critical layers over ocean waves. *J. Phys. Oceanogr.*, **43**, 2156–2172, doi:10.1175/JPO-D-13-056.1.
- , W. L. Peirson, H. Branger, J. W. Walker, J.-P. Giovanangeli, and V. Makin, 2013b: Growth and dissipation of wind-forced, deep-water waves. *J. Fluid Mech.*, **722**, 5–50, doi:10.1017/jfm.2013.88.
- Hara, T., and S. E. Belcher, 2002: Wind forcing in the equilibrium range of wind-wave spectra. *J. Fluid Mech.*, **470**, 223–245, doi:10.1017/S0022112002001945.
- , and P. P. Sullivan, 2015: Wave boundary layer turbulence over surface waves in a strongly forced condition. *J. Phys. Oceanogr.*, **45**, 868–883, doi:10.1175/JPO-D-14-0116.1.
- Hristov, T., C. Friehe, and S. Miller, 1998: Wave-coherent fields in air flow over ocean waves: Identification of cooperative behavior buried in turbulence. *Phys. Rev. Lett.*, **81**, 5245, doi:10.1103/PhysRevLett.81.5245.
- , S. Miller, and C. Friehe, 2003: Dynamical coupling of wind and ocean waves through wave-induced air flow. *Nature*, **422**, 55–58, doi:10.1038/nature01382.
- Hsu, C.-T., E. Y. Hsu, and R. L. Street, 1981: On the structure of turbulent flow over a progressive water wave: theory and experiment in a transformed, wave-following co-ordinate system. *J. Fluid Mech.*, **105**, 87–117, doi:10.1017/S0022112081003121.
- Jiménez, J., 2012: Cascades in wall-bounded turbulence. *Annu. Rev. Fluid Mech.*, **44**, 27–45, doi:10.1146/annurev-fluid-120710-101039.
- Jones, I. S., and Y. Toba, 2001: *Wind Stress over the Ocean*. Cambridge University Press, 328 pp.
- Kawai, S., 1981: Visualization of airflow separation over wind-wave crests under moderate wind. *Bound.-Layer Meteor.*, **21**, 93–104, doi:10.1007/BF00119370.
- Kawamura, H., and Y. Toba, 1988: Ordered motion in the turbulent boundary layer over wind waves. *J. Fluid Mech.*, **197**, 105–135, doi:10.1017/S0022112088003192.
- Kendall, J. M., 1970: The turbulent boundary layer over a wall with progressive surface waves. *J. Fluid Mech.*, **41**, 259–281, doi:10.1017/S0022112070000617.
- Kihara, N., H. Hanazaki, T. Mizuya, and H. Ueda, 2007: Relationship between airflow at the critical height and momentum transfer to the traveling waves. *Phys. Fluids*, **19**, 015102, doi:10.1063/1.2409736.
- Kim, H., S. Kline, and W. Reynolds, 1971: The production of turbulence near a smooth wall in a turbulent boundary layer. *J. Fluid Mech.*, **50**, 133–160, doi:10.1017/S0022112071002490.
- Kline, S., W. Reynolds, F. Schraub, and P. Runstadler, 1967: The structure of turbulent boundary layers. *J. Fluid Mech.*, **30**, 741–773, doi:10.1017/S0022112067001740.
- Kovaszny, L. S., 1970: The turbulent boundary layer. *Annu. Rev. Fluid Mech.*, **2**, 95–112, doi:10.1146/annurev.fl.02.010170.000523.
- Lin, M.-Y., C.-H. Moeng, W.-T. Tsai, P. P. Sullivan, and S. E. Belcher, 2008: Direct numerical simulation of wind-wave generation processes. *J. Fluid Mech.*, **616**, 1–30, doi:10.1017/S0022112008004060.
- Longuet-Higgins, M. S., 1969: Action of a variable stress at the surface of water waves. *Phys. Fluids*, **12**, 737–740, doi:10.1063/1.1692549.
- Makin, V., V. Kudryavtsev, and C. Mastenbroek, 1995: Drag of the sea surface. *Bound.-Layer Meteor.*, **73**, 159–182, doi:10.1007/BF00708935.

- Mastenbroek, C., V. Makin, M. Garat, and J.-P. Giovanangeli, 1996: Experimental evidence of the rapid distortion of turbulence in the air flow over water waves. *J. Fluid Mech.*, **318**, 273–302, doi:10.1017/S0022112096007124.
- Meinhart, C. D., and R. J. Adrian, 1995: On the existence of uniform momentum zones in a turbulent boundary layer. *Phys. Fluids*, **7**, 694–696, doi:10.1063/1.868594.
- Melville, W. K., 1983: Wave modulation and breakdown. *J. Fluid Mech.*, **128**, 489–506, doi:10.1017/S0022112083000579.
- Miles, J. W., 1957: On the generation of surface waves by shear flows. *J. Fluid Mech.*, **3**, 185–204, doi:10.1017/S0022112057000567.
- , 1959: On the generation of surface waves by shear flows: Part 3. Kelvin-Helmholtz instability. *J. Fluid Mech.*, **6**, 583–598, doi:10.1017/S0022112059000842.
- Miles, J., 1993: Surface-wave generation revisited. *J. Fluid Mech.*, **256**, 427–441, doi:10.1017/S0022112093002836.
- Miller, M., T. Nennstiel, J. H. Duncan, A. A. Dimas, and S. Pröstler, 1999: Incipient breaking of steady waves in the presence of surface wakes. *J. Fluid Mech.*, **383**, 285–305, doi:10.1017/S0022112098004029.
- Mueller, J. A., and F. Veron, 2009: Nonlinear formulation of the bulk surface stress over breaking waves: Feedback mechanisms from air-flow separation. *Bound.-Layer Meteor.*, **130**, 117–134, doi:10.1007/s10546-008-9334-6.
- Okuda, K., S. Kawai, and Y. Toba, 1977: Measurement of skin friction distribution along the surface of wind waves. *J. Oceanogr. Soc. Japan*, **33**, 190–198, doi:10.1007/BF02109691.
- Oppenheim, A. V., and R. W. Schaffer, 2013: *Discrete-Time Signal Processing*. 3rd ed. Pearson Education, 1120 pp.
- Perlin, M., W. Choi, and Z. Tian, 2013: Breaking waves in deep and intermediate waters. *Annu. Rev. Fluid Mech.*, **45**, 115–145, doi:10.1146/annurev-fluid-011212-140721.
- Phillips, O. M., 1957: On the generation of waves by turbulent wind. *J. Fluid Mech.*, **2**, 417–445, doi:10.1017/S0022112057000233.
- , 1977: *Dynamics of the Upper Ocean*. 2nd ed. Cambridge University Press, 336 pp.
- Raffel, M., C. E. Willert, S. T. Wereley, and J. Kompenhans, 2007: *Particle Image Velocimetry: A Practical Guide*. 2nd ed. Springer, 448 pp.
- Reul, N., H. Branger, and J. P. Giovanangeli, 1999: Air flow separation over unsteady breaking waves. *Phys. Fluids*, **11**, 1959–1961, doi:10.1063/1.870058.
- , —, and J.-P. Giovanangeli, 2008: Air flow structure over short-gravity breaking water waves. *Bound.-Layer Meteor.*, **126**, 477–505, doi:10.1007/s10546-007-9240-3.
- Robinson, S. K., 1991: Coherent motions in the turbulent boundary layer. *Annu. Rev. Fluid Mech.*, **23**, 601–639, doi:10.1146/annurev.fl.23.010191.003125.
- Schlichting, H., and K. Gersten, 2000: *Boundary-Layer Theory*. 8th ed. Springer, 799 pp.
- Simpson, R. L., 1989: Turbulent boundary-layer separation. *Annu. Rev. Fluid Mech.*, **21**, 205–232, doi:10.1146/annurev.fl.21.010189.001225.
- Smedman, A., U. Höglström, H. Bergström, A. Rutgersson, K. K. Kahma, and H. Pettersson, 1999: A case study of air-sea interaction during swell conditions. *J. Geophys. Res.*, **104**, 25 833–25 851, doi:10.1029/1999JC900213.
- Sullivan, P. P., and J. C. McWilliams, 2010: Dynamics of winds and currents coupled to surface waves. *Annu. Rev. Fluid Mech.*, **42**, 19–42, doi:10.1146/annurev-fluid-121108-145541.
- , —, and C. H. Moeng, 2000: Simulation of turbulent flow over idealized water waves. *J. Fluid Mech.*, **404**, 47–85, doi:10.1017/S0022112099006965.
- , J. B. Edson, T. Hristov, and J. C. McWilliams, 2008: Large-eddy simulations and observations of atmospheric marine boundary layers above nonequilibrium surface waves. *J. Atmos. Sci.*, **65**, 1225–1245, doi:10.1175/2007JAS2427.1.
- , J. C. McWilliams, and E. G. Patton, 2014: Large-eddy simulation of marine atmospheric boundary layers above a spectrum of moving waves. *J. Atmos. Sci.*, **71**, 4001–4027, doi:10.1175/JAS-D-14-0095.1.
- Thomas, M., S. Misra, C. Kambhamettu, and J. Kirby, 2005: A robust motion estimation algorithm for PIV. *Meas. Sci. Technol.*, **16**, 865–877, doi:10.1088/0957-0233/16/3/031.
- Veron, F., G. Saxena, and S. K. Misra, 2007: Measurements of the viscous tangential stress in the airflow above wind waves. *Geophys. Res. Lett.*, **34**, 1959–1961, doi:10.1029/2007GL031242.
- Wallace, J. M., H. Eckelmann, and R. S. Brodkey, 1972: The wall region in turbulent shear flow. *J. Fluid Mech.*, **54**, 39–48, doi:10.1017/S0022112072000515.
- Webster, P. J., and R. Lukas, 1992: TOGA COARE: The coupled ocean-atmosphere response experiment. *Bull. Amer. Meteor. Soc.*, **73**, 1377–1416, doi:10.1175/1520-0477(1992)073<1377:TCTCOR>2.0.CO;2.
- Willmarth, W., and S. Lu, 1972: Structure of the Reynolds stress near the wall. *J. Fluid Mech.*, **55**, 65–92, doi:10.1017/S002211207200165X.
- Wu, J., 1975: Wind-induced drift currents. *J. Fluid Mech.*, **68**, 49–70, doi:10.1017/S0022112075000687.
- Wu, J.-Z., H.-Y. Ma, and M. D. Zhou, 2006: *Vorticity and Vortex Dynamics*. Springer, 776 pp.
- Yang, D., and L. Shen, 2010: Direct-simulation-based study of turbulent flow over various wavy boundaries. *J. Fluid Mech.*, **650**, 131–180, doi:10.1017/S0022112009993557.
- Yao, A., and C. H. Wu, 2005: Incipient breaking of unsteady waves on sheared currents. *Phys. Fluids*, **17**, 082104, doi:10.1063/1.2000276.